# Nonlinear estimation of geometric parameters in FEMs of volcano deformation: Integrating tomography models and geodetic data for Okmok volcano, Alaska

Timothy Masterlark,[1] Kurt L. Feigl,[2] Matthew Haney,[3] Jonathan Stone,[1] Clifford Thurber,[2] and Erika Ronchin[4]

Received 25 August 2011; revised 15 December 2011; accepted 19 December 2011; published 23 February 2012.

[1] The internal structure, loading processes, and effective boundary conditions of a volcano control the deformation observed at the Earth's surface. Using finite element models (FEMs), we simulate the response due to a pressurized magma chamber embedded in a domain having a distribution of elastic material properties. We present the Pinned Mesh Perturbation method (PMP) to automate the mesh generation process in response to perturbations of the position of a simulated magma chamber within an FEM domain. Using InSAR-observed deformation for the 1997 eruption of Okmok volcano, Alaska, as an example, we combine PMP with nested Monte Carlo methods to estimate a set of linear and nonlinear parameters that characterize the depressurization and location of the magma chamber beneath Okmok's caldera. The three-dimensional FEMs used in the PMP method simulate the distribution of material properties of tomography models and account for the irregular geometry of the topography and bathymetry. The estimated depth of an assumed spherical magma chamber is $3527^{+55}_{-54}$ m below sea level and is sensitive to the distribution of material properties. This depth is consistent with lithostatic pressure constraints and very long period tremor observations. The fit of this FEM to the InSAR data is a significant improvement, at the 95% confidence level, compared to the fit of a corresponding FEM having homogeneous material properties. The methods presented here allow us to construct deformation models that integrate tomography models with geodetic observations, in an effort to achieve a deeper understanding of active volcanoes.

**Citation:** Masterlark, T., K. L. Feigl, M. Haney, J. Stone, C. Thurber, and E. Ronchin (2012), Nonlinear estimation of geometric parameters in FEMs of volcano deformation: Integrating tomography models and geodetic data for Okmok volcano, Alaska, *J. Geophys. Res.*, *117*, B02407, doi:10.1029/2011JB008811.

## 1. Introduction

### 1.1. Volcano Deformation Models

[2] The migration and storage of magma within an active volcano produce a deformation signature on the Earth's surface. The internal structure of a volcano and specific movements of the magma control the details of the deformation field. Geodetic data can map this deformation and data from a local array of seismic instruments can image the internal structure. Numerical models simulate the response due to magma migration and storage within this internal structure, thus linking the surface deformation to the movements of magma at depth. By simulating the magma intrusion —the *impulse*— with numerical models, and comparing predicted to observed deformation —the *response*, we can quantify parameters that describe the magma intrusion. Forward models allow us to predict the surface deformation based on the specific characteristics of a magma chamber, such as the location, geometry, and pressure changes in both space and time. To refine these models, however, we must solve the inverse problem to estimate (calibrate) characteristic parameters of a magma chamber based on observed surface deformation (calibration targets). Nonetheless, the specific model configuration, a prerequisite for both forward and inverse analyses, may strongly influence results and interpretations.

#### 1.1.1. Half-Space Models

[3] Relatively simple analytical solutions for deformation sources embedded in a homogeneous elastic half-space (HEHS) are commonly used to simulate observed volcano deformation because they are computationally inexpensive and can easily be integrated into inverse analyses that seek to characterize the geometry, position, and magnitude of a deformation source. Analytical solutions are available for a variety of source geometries in HEHS domains (e.g., point

[1]Department of Geological Sciences, University of Alabama, Tuscaloosa, Alabama, USA.
[2]Department of Geoscience, University of Wisconsin–Madison, Madison, Wisconsin, USA.
[3]Alaska Volcano Observatory, U.S. Geological Survey, Anchorage, Alaska, USA.
[4]Institute of Earth Sciences Jaume Almera, CSIC, Barcelona, Spain.

Copyright 2012 by the American Geophysical Union.
0148-0227/12/2011JB008811

sources and spheres [*McTigue*, 1987; *Mogi*, 1958]; spheroids [*Yang et al.*, 1988]; and faults, dikes, and sills [*Okada*, 1992]) to account for corresponding characteristic deformation patterns. Complicated deformation patterns are accounted for by superposition of multiple deformation sources or variable source magnitudes over a partitioned source entity [e.g., *Lundgren and Rosen*, 2003; *Vasco et al.*, 2002; *Wright et al.*, 2006]. However, the reliability of the estimated source parameters, and thus any resulting interpretations, hinges on the validity of the underlying assumptions. In particular, HEHS models imply that the material properties of a volcano are elastic, the values of the two elastic moduli are spatially uniform, and the land surface is flat (e.g., negligible topographic or bathymetric relief).

#### 1.1.2. Beyond Half-Space Models

[4] Finite element models (FEMs) are the only known type of mathematical model capable of satisfying the elastic equations over domains with arbitrary geometric configurations and spatially variable material properties. Such models can simulate pressurized magma chambers (a deformation source) embedded in domains having a distribution of material properties and the irregular relief of a volcano. In spite of their ability to simulate complex deformation systems, FEMs contain two inherent obstacles to nonlinear inverse estimations of the parameters describing the location and geometry of the deformation source. First, the FEM mesh is geometry-dependent and must be redefined for any changes to the position or geometry of the deformation source. Mesh construction requires careful design, testing, and validation to ensure that the mesh configuration leads to an acceptable solution. The ability to impose automatic source parameter perturbations and subsequently reconstruct an acceptable mesh is critical to advancing nonlinear FEM-based inverse analyses of volcano deformation [*Masterlark et al.*, 2006]. Second, computational requirements of FEMs are much greater than those for analytical solutions. It is essential to minimize the computational time for an FEM embedded in an iterative inverse scheme. Ultimately, the computational performance of the hardware limits the feasibility of embedding FEMs in nonlinear inverse analyses, because each set of parameter perturbations requires both re-meshing and a recomputation of an FEM. The aim of this paper is to demonstrate how FEMs can be embedded in fully automated nonlinear inverse methods that estimate the optimal parameters for the horizontal position, depth, and pressurization of a spherical magma chamber, based on geodetic data. These methods will satisfy the requirement for automated re-meshing that is necessary for iterative perturbations of the parameters that describe the geometry of the system for computationally feasible three-dimensional FEMs.

### 1.2. Study Site: Okmok Volcano, Alaska

#### 1.2.1. Tectonic Setting

[5] The 3,000 km-long Aleutian volcanic arc extends from Alaska to Kamchatka and hosts more than 40 active volcanoes [*Begét et al.*, 2005; *Finney et al.*, 2008]. The arc was built from volcanic and tectonic activity that represents the surface expression of the subduction of the Pacific Plate beneath the overriding North American Plate [*Fournelle et al.*, 1994]. The plate convergence along the arc varies from 66 mm/yr (orthogonal along the east end of the arc) to 72 mm/yr (trench-parallel along the west end of the arc) [*Cross and Freymueller*, 2008]. Umnak Island is located in the central Aleutian arc and is primarily mafic with an oceanic crustal basement [*House and Jacob*, 1983]. The island is adjacent to a weakly coupled portion of the plate boundary and GPS data indicate that the tectonic strain rate across Umnak Island is less than 100 nanostrain/yr [*Cross and Freymueller*, 2008].

[6] Umnak Island includes two volcanic lobes aligned with the trench and separated by an isthmus. Okmok volcano (Figure 1), which occupies the northeast lobe of Umnak Island, is one of the largest volcanic shields of the Aleutian arc [*Burgisser*, 2005; *Larsen et al.*, 2007]. A central caldera, having a radius of 5 km, dominates the physiography of Okmok volcano. The rim of this caldera has an elevation of about 900 m above sea level (asl) and the elevation of the caldera floor is about 400 m asl. The existing caldera is the result of two separate caldera-forming eruptions, for which radiogenic measurements indicate ages of 12,000 and 2,050 years [*Finney et al.*, 2008; *Larsen et al.*, 2007]. Post-caldera eruptions, which generally emanate from intracaldera cones, are effusive and basaltic [*Burgisser*, 2005]. The most recent eruption in 2008 originated from several new vents surrounding Cone D near the eastern rim of the caldera, while the three previous eruptions in 1945, 1958, and 1997 originated from Cone A near the southwest rim of the caldera [*Larsen et al.*, 2009] (Figure 1). Geochemical analyses of erupted materials are consistent with primitive magma from depth and brief storage in shallow reservoirs [*Finney et al.*, 2008]. Over the past decade, Okmok was instrumented with GPS instruments [*Fournier et al.*, 2009; *Miyagi et al.*, 2004] and seismic networks [*Caplan-Auerbach et al.*, 2004; *Haney*, 2010; *Johnson et al.*, 2010; *Masterlark et al.*, 2010]. Remote sensing data remain essential for monitoring Okmok, due to the relatively remote location of the volcano [*Dehn et al.*, 2000; *Lu et al.*, 2003; *Lu*, 2007; *Patrick et al.*, 2004].

[7] The deformation associated with the 1997 eruption of Okmok is used to demonstrate the techniques developed in this study. This eruption began on 11 February 1997 with steam and ash plumes and progressed to a moderate Strombolian eruption, producing explosive ash plumes and lava flows emanating from Cone A that flowed toward the center of the caldera (Figure 1) [*Miller et al.*, 1998]. Thermal anomalies in Okmok caldera were observed with Advanced Very High Resolution Radiometer (AVHRR) imagery during February and March 1997 [*Dehn et al.*, 2000; *Patrick et al.*, 2004]. The eruption ended 23 May 1997 [*McGimsey and Wallace*, 1999], giving a total eruption interval of 101 days. Based on interferometric synthetic aperture radar (InSAR) measurements, the net volume of the 1997 lava flow is $0.154 \pm 0.025$ km$^3$ and has a maximum thickness of 50 m [*Lu et al.*, 2003].

#### 1.2.2. Data

[8] The available data are separated into two categories, based on usage from a modeling perspective. Constraining data are treated as a priori information and are built into the models. Calibration targets (data) are used to estimate the calibration (or adjustable) parameters. For this study, topography and bathymetry constrain the geometry of the free surface and ambient noise tomography and regional velocity models constrain the distribution of material properties within the model domain. InSAR data serve as

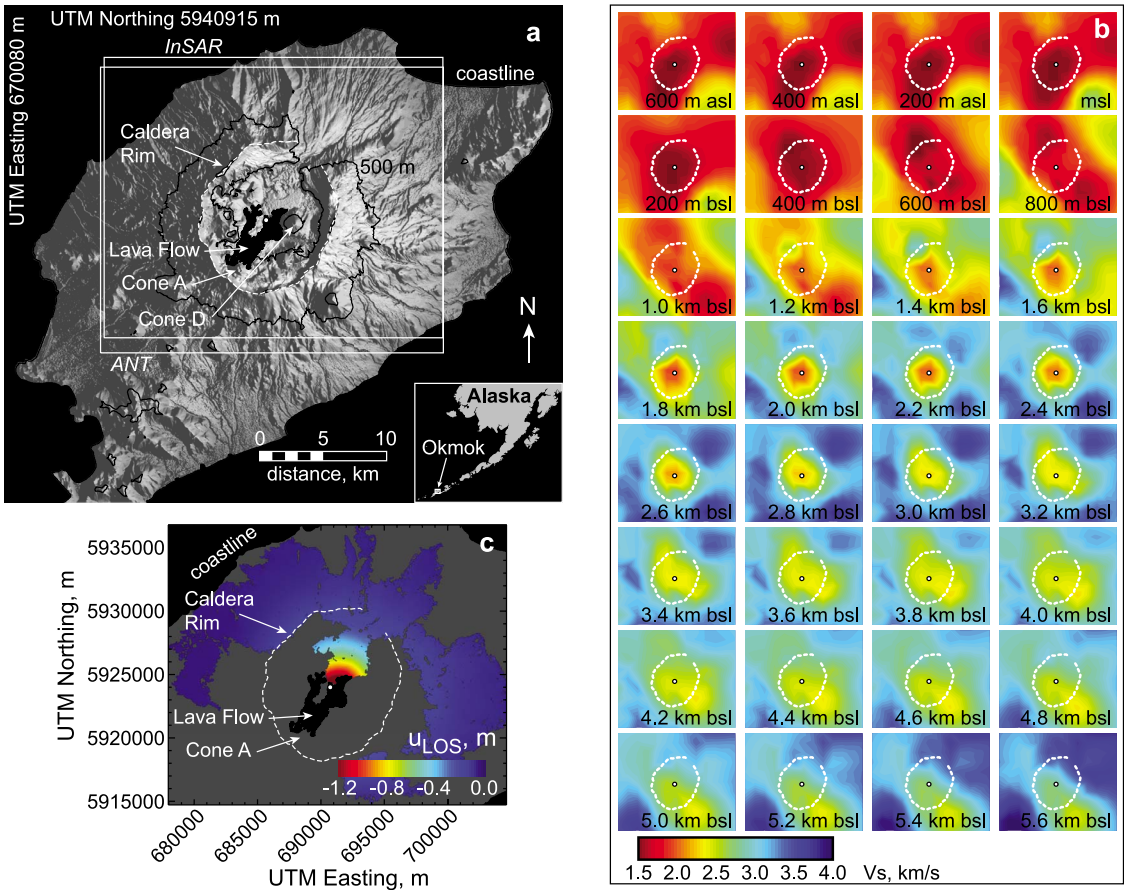


**Figure 1.** Okmok volcano, Alaska. (a) Physiography. The black region in the caldera is the footprint of the lava flow from the 1997 eruption [*Lu et al.*, 2003]. The white dashed line is the caldera rim. The small white circle at the center of the caldera shows the initial estimated location of the deformation source. Inset at bottom right shows the location of Okmok in the Aleutian Arc. (b) Internal structure determined from ambient noise tomography (ANT) [*Masterlark et al.*, 2010]. The shear wave distribution is shown for the depth indicated in the bottom of each plot. (c) Unwrapped InSAR data for the 1997 eruption.

calibration targets, which are used in inverse methods to calibrate parameters describing the position and pressurization of a deformation source.

[9] *Lu et al.* [2003] used synthetic aperture radar to develop a digital elevation model (DEM) for the entire northeast lobe of Umnak Island that is occupied by Okmok. The original DEM had a pixel resolution of 5 m and vertical uncertainty of 10 m. This DEM was re-sampled to correspond to the 40-m pixel resolution of the InSAR image described below (Figure 1). We supplement this DEM with coarse-resolution (1-min) topography and bathymetry data available from the NOAA National Geophysical Data Center (http://www.ngdc.noaa.gov) to develop a DEM describing the geometry of the Earth's surface for both onshore and offshore regions of the model domain.

[10] Ambient noise tomography (ANT) reveals a complex internal structure for Okmok volcano (Figure 1b) and *Masterlark et al.* [2010] provide a detailed analysis. In particular, ANT indicates two low velocity zones (LVZs). The shallow LVZ fills the caldera from the land surface to about 1000 m below sea level (bsl). A deeper LVZ suggests the presence of a magma chamber having a center at a depth of about 4000 m bsl. It will be shown that the shallow LVZ strongly influences the estimated depth of the magma chamber, while the deep LVZ verifies the estimated depth of the magma chamber.

[11] For our analysis, we use InSAR data with image-pair acquisition dates of 9 October 1995 and 9 September 1997, which span the 1997 eruption of Okmok volcano (Image ID 66 from *Lu et al.* [2005]). An overview of the InSAR data is given here and summarized in Table 1. Details of the InSAR processing are given by *Lu et al.* [2005]. The InSAR data map the volcano-wide deflation of Okmok (Figure 1c). The average line-of-sight vector is $\mathbf{L} = [0.346, -0.081, 0.935]$. The deformation pattern is strongly symmetric about a vertical axis centered on the caldera and has a maximum line-of-sight displacement of about $-1.4$ m. Several studies confirm that a spherical deformation source beneath the center of the caldera, which predicts radially symmetric deformation, well fits the InSAR data [*Lu et al.*, 2000, 2005; *Mann et al.*, 2002; *Masterlark*, 2007; *Masterlark et al.*, 2010], although we note that these results are non-unique.

[12] We ignore deformation between the initial SAR image acquisition date (9 October 1995) and the beginning of the 1997 eruption (11 February 1997). If we assume the magma supply is a linear function of the pressure gradient

**Table 1.** InSAR Data Summary

| Aspect | Specifications |
|---|---|
| Image 1 | ERS-1/Orbit 22147/09 October 1995 |
| Image 2 | ERS-2/Orbit 12494/09 September 1997 |
| Wavelength | C-band/0.0283 m |
| Track | 115 |
| Pass | descending |
| Baseline | 8 m |
| **L** (line-of-sight), [east,north,up] | [0.346, −0.081, 0.935] |
| Columns | 1100 |
| Rows | 980 |
| Pixel dimensions | 40 m × 40 m |
| *N* (coherent pixels) | 115,550 |
| Reference position (top-left corner of image) | UTM zone 2, Easting 670080 m, Northing 5940915 m |

between a deep magma source with constant pressure and the shallow magma chamber, then the pre-eruption magma flux into the chamber diminishes with the pressure gradient between the shallow magma chamber and deep magma source [*Dvorak and Okamura*, 1987; *Turcotte and Schubert*, 2002]. InSAR data confirm that magma intrusion into a shallow chamber was negligible during 1995–1996 [*Lu et al.*, 2005]. Furthermore, we assume that the deformation between the end of the 1997 eruption (23 May 1997) and the acquisition of the second SAR image (9 September 1997) is minimal. *Masterlark et al.* [2010] suggested that the deformation during this post-eruption interval is due to viscoelastic relaxation and represents about 10% of the total signal. Because a primary focus of this study is to identify the position of the deformation source rather than the temporal behavior of the source strength, we restrict our analysis to elastic models and assume a static pressurization of the magma chamber during the interval spanned by the InSAR image pair.

[13] We use the deformation data associated with 1997 eruption of Okmok volcano for two reasons. First, the InSAR data have a high signal-to-noise ratio and the overall pattern of deformation is well predicted by relatively simple models simulating pressurization of a spherical deformation source. Second, the InSAR data from the 1997 eruption are well studied. No fewer than five published studies estimated deformation source parameters for the 1997 eruption of Okmok using InSAR [*Lu et al.*, 2000, 2005; *Mann et al.*, 2002; *Masterlark*, 2007; *Masterlark et al.*, 2010]. By using the same deformation (InSAR) data, we can compare results and interpretations from this study, with its relatively sophisticated model configurations, to results and interpretations from earlier studies that were based on simple HEHS models. Such comparisons reveal variations in results and interpretations that are directly attributed to the specific configuration of a given deformation model.

[14] The remainder of this paper comprises three sections that are structured to follow a deformation modeling protocol [*Masterlark and Hughes*, 2008]. First, in the Methods section, we describe the configuration, construction, and validation of the FEMs. This section goes on to describe the implementation of a parameter optimization method that allows for automated FEM re-builds for the nonlinear parameters. Second, we present results of the parameter optimization for FEMs that simulate the complex internal structure of the volcano, as well as for FEMs that simulate a uniform internal structure. We compare model predictions to observations that are independent of the calibration process to verify the model. Third, we discuss comparisons of results from alternative FEM configurations in this analysis, as well as results from previous analyses. Finally, we present conclusions and recommendations.

## 2. Methods

### 2.1. Deformation Models

[15] The active magmatic system of Okmok likely includes a temperature-dependent rheologic structure, a system of hydrothermal fluids, and a complex internal assembly of lava and pyroclastic flows and intrusive magma bodies [*Finney et al.*, 2008; *Masterlark et al.*, 2010; *Walker*, 1993], all of which translate to localized weaknesses in the crust. Furthermore, the topographic relief of Okmok volcano invalidates the flat land surface assumption of HEHS models. It is well known that the HEHS assumptions can strongly influence both source parameter estimations and forward model predictions for deformation and stress in volcanic deformation systems [e.g., *Masterlark et al.*, 2010, and references therein]. Accordingly, we conclude that the HEHS assumptions poorly approximate Okmok volcano and we turn, instead, to the flexibility of FEMs to simulate the deformation of Okmok volcano.

#### 2.1.1. FEM Method

[16] We construct FEMs to simulate the deformation of Okmok volcano resulting from pressurization of a magma chamber embedded in an elastic model domain. We use the resulting FEM predictions to estimate the four parameters that best describe the position and change in pressure of the magma chamber. All FEMs in this analysis are constructed using Abaqus (version 6.9-EF, Dassault Systèmes Simulia Corp., Providence, Rhode Island, 2009, available at http://www.simulia.com). Expressed in index notation, the governing equations for a three-dimensional elastic domain having spatially variable (heterogeneous) material properties are:

$$\frac{\partial}{\partial x_i}\left[2G\left(\frac{\partial u_i}{\partial x_i}+\frac{\upsilon}{1-2\upsilon}\nabla\cdot\mathbf{u}\right)\right]+\frac{\partial}{\partial x_j}\left[G\left(\frac{\partial u_i}{\partial x_j}+\frac{\partial u_j}{\partial x_i}\right)\right]=0 \quad (1)$$

where $u$ is displacement, $G$ is the shear modulus, and $\upsilon$ is Poisson's ratio. The subscripts $i$ and $j$ span orthogonal direction components 1, 2, and 3, and $i \neq j$. If the material properties are homogeneous over the domain, then equation (1) reduces to the Navier equations [*Sadd*, 2010]. In this formulation, $x_1$, $x_2$, and $x_3$ are equivalent to Cartesian coordinates $x$, $y$, and $z$ (easting, northing, and vertical), respectively. Similarly, $u_1$, $u_2$, and $u_3$ are equivalent to $u_x$, $u_y$, and $u_z$, respectively. Coordinate positions are given in Universal Transverse Mercator (UTM) projection with respect to an origin defined as the center of the caldera and zero m asl (Table 2).

[17] The model domain configuration is given in Figure 2 and summarized in Table 2. The three-dimensional model domain approximates a solid hemisphere centered on the caldera and having a radius of 60 km. The outer surface of

**Table 2.** FEM Configuration

| Aspect | Specifications |
|---|---|
| Domain space origin | $x = 0$ at UTM zone 2 Easting 690719 m, $y = 0$ at UTM zone 2 Northing 5923980 m, $z = 0$ at mean sea level |
| $\mathbf{S}_0$ | [0, 0, −3000 m] |
| VAL | |
| Analysis type | elastic |
| Elements (1st order tetrahedra) | 76,606 |
| Nodes | 13,870 |
| Total FEM variables | 41,610 |
| Maximum domain depth | 60 km |
| Maximum domain radius | 60 km |
| Chamber radius ($r_S$) | 1000 m |
| Radius of effective sphere ($r_{S_{eff}}$) | 995.930 m |
| Volume of effective sphere | $4.137853 \times 10^9$ m$^3$ |
| $G$ | 20 GPa |
| $\upsilon$ | 0.25 |
| $\Delta P$ | 50 MPa |
| Far-field boundary conditions | zero displacement |
| Top of model domain | free surface, flat |
| HET and HOM | |
| Analysis type | elastic |
| Elements (1st order tetrahedra) | 86,875 |
| Nodes | 15,722 |
| Total FEM variables | 47,166 |
| Maximum domain depth | 60 km |
| Maximum domain radius | 60 km |
| Chamber radius ($r_S$) | 1000 m |
| Radius of effective sphere ($r_{S_{eff}}$) | 995.16 m |
| $\Delta P_0$ | 10 MPa |
| Far-field boundary conditions | zero displacement |
| Top of model domain | free surface (topography) |
| Unique to HET | |
| Chamber volume ($V$) | $4.128291 \times 10^9$ m$^3$ |
| $E$ | distribution (Figure 2c) |
| $\upsilon$ (other than LVZ) | 0.29 |
| $\upsilon$ (LVZ) | 0.15 |
| Unique to HOM | |
| Chamber volume ($V$) | $4.128264 \times 10^9$ m$^3$ |
| $E$ | $5.0 \times 10^{10}$ Pa |
| $\upsilon$ | 0.25 |
| Auxiliary FEM | |
| Analysis type | $\nabla^2 E = 0$ |
| Mesh | same as HET |
| Internal boundary conditions | interpolated from seismic tomography |
| Far field boundary conditions | interpolated from layered $V_s$ model. |
| CORE | |
| Analysis type | elastic |
| Elements (1st order tetrahedra) | 34,058 |
| Nodes | 6,397 |
| Total FEM variables | 19,191 |
| Domain height | ~9 km |
| Domain radius | 8 km |

the hemisphere represents the far-field lateral and depth extent of the domain. The top of the domain has a geometry that represents the topography of the land surface and bathymetry of the seafloor. The domain includes a partition for a subcaldera core, which houses the simulated magma chamber. This cylindrical core has a diameter of 8000 m and a height of 9000 m (from $z = -9000$ m to $z = 0$ m) plus the additional height associated with topography (Figure 2). The magma chamber is simulated as a pressurized spherical cavity with a radius of 1000 m. We do not imply that the actual magma chamber in Okmok is a spherical cavity. Instead, we recognize that the magma chamber of Okmok is most likely a complex assembly of various conduits and reservoirs whose net behavior as a deformation source is well approximated by a pressurized sphere. The entire domain is tessellated into first order tetrahedral elements. Characteristic lengths of elements are about 175 m near the magma chamber and gradually increase to characteristic lengths of about 8000 m near the far-field boundaries. Initial conditions are static equilibrium. We assume that the far-field surfaces of the model domain are sufficiently far away from the caldera such that displacements vanish and we specify zero displacement boundary conditions along these surfaces. This assumption is validated later. The top of the model domain, representing the land surface and seafloor, is a stress-free surface. The impulse change in pressure along the walls of the magma chamber is $\Delta P_0$. Because this is an elastic system, the deformation throughout the domain is a linear function of $\Delta P_0$.

#### 2.1.2. Pinned Mesh Perturbation

[18] The Pinned Mesh Perturbation (PMP) method employs a reduced basis [*Huebner et al.*, 2001] that uses an auxiliary FEM to generate geometric perturbations to an initial mesh. Strategic geometric features of this mesh are subject to a combination of both zero displacement (pinned) and nonzero displacement (perturbation) specifications. The auxiliary FEM satisfies equation (1) for the imposed boundary conditions, thereby distributing the mesh distortion over the domain. We use PMP to generate the complex geometry of topographic and bathymetric relief for the free surface, as well as to automate the re-meshing process necessary to perturb the position of the magma chamber. Automatic re-meshing is required in any iterative scheme that estimates parameters related to variable nodal positions.

[19] We implement the PMP method for Abaqus using a four-step process. First, we construct an initial domain geometry and mesh for an elastic FEM. This initial configuration must be carefully designed to accommodate the desired distortions, while simultaneously maintaining a valid mesh. Second, we specify displacements as boundary conditions to preserve the general shape of the domain and achieve the desired geometric perturbation from the initial configuration. Nodal displacements for the entire mesh are calculated for an elastic material in response to the specified displacements. Third, the nodal positions for the initial mesh are adjusted by these calculated displacements (design vectors) to form a new mesh having the desired geometry [*Huebner et al.*, 2001]:

$$\mathbf{N} = \mathbf{N}_0 + \mathbf{U} \tag{2}$$

where $\mathbf{N}_0$ and $\mathbf{N}$ are matrices of nodal definitions for the initial and final FEM meshes, respectively, and $\mathbf{U}$ is a matrix of design vectors (Figure 3). The $i$th rows in $\mathbf{N}_0$, $\mathbf{N}$, and $\mathbf{U}$ are [(*node name*)$_i$, $x_i$, $y_i$, $z_i$], [(*node name*)$_i$, $x_i$, $y_i$, $z_i$], and [0, $u_{x,i}$, $u_{y,i}$, $u_{z,i}$], respectively. Each node in Abaqus is identified by a unique integer from 1 to 999999999 (the node name). Note that in this formulation, the null element in $\mathbf{U}$ preserves the node name given in $\mathbf{N}_0$, while the nodal coordinates for a given node name may vary. Because

element geometry in Abaqus is defined in terms of invariant node names, the method efficiently re-meshes the model domain with each perturbation. Fourth, the elements in the resulting mesh are tested for quality.

[20] We first apply PMP to account for the irregular surface associated with topography and bathymetry. We construct a prototype configuration that has the geometric components of the FEM configuration discussed above, but having a flat free surface with an additional first-order approximation of the caldera rim to reduce anticipated distortion of the important geometric features. We then apply appropriate boundary conditions to preserve certain geometric features, such as the spherical cavity and the walls and floor of the subcaldera core, while simultaneously perturbing the geometry of the free surface according to the difference between the prototype free surface configuration and the DEM. We then calculate nodal displacements over the domain and adjust the nodal positions using equation (2). This process defines a mesh that includes a spherical cavity embedded in a subcaldera core that is in turn embedded in a domain having a top surface with the irregular geometry of the topographic and bathymetric relief. We will use this mesh for an FEM configuration called HET (Figure 2b). Although a previous study indicated that the effects of topography and bathymetry on deformation predictions are not important for Okmok volcano [*Masterlark*, 2007], the PMP method will be useful for constructing deformation models for other Alaskan volcanoes that have substantial topographic relief, such as Augustine or Redoubt.

[21] Our second application of PMP imposes the three-dimensional perturbations to the position of a pressurized spherical cavity that represents the magma chamber. This implementation is embedded in a fully automated Monte Carlo optimization algorithm that estimates the position and pressurization parameters that minimize the misfit between model predictions and InSAR data. The predicted deformation is a nonlinear function of the three-component vector **S**, which describes the position of the magma chamber.

[22] We construct an auxiliary FEM of the subcaldera core (defined as CORE, Figure 2d) by duplicating the subcaldera core partition from the mesh of HET. The outer surfaces of CORE have zero displacement boundary conditions. All nodes of the spherical cavity that represents the magma chamber have specified displacements corresponding to a three-component perturbation vector. The nodal displacements over the domain satisfy the elastic governing equation (1). Nodal positions for the perturbed mesh are calculated from equation (2) and the resulting mesh is inserted into HET.

[23] The PMP method allows us to change the position of the chamber in an FEM by specifying a parameterized three-component perturbation vector. However, if we change the position too much, then the mesh will become overly distorted. Because the surface area of the simulated magma chamber is much smaller than the surface area of the core

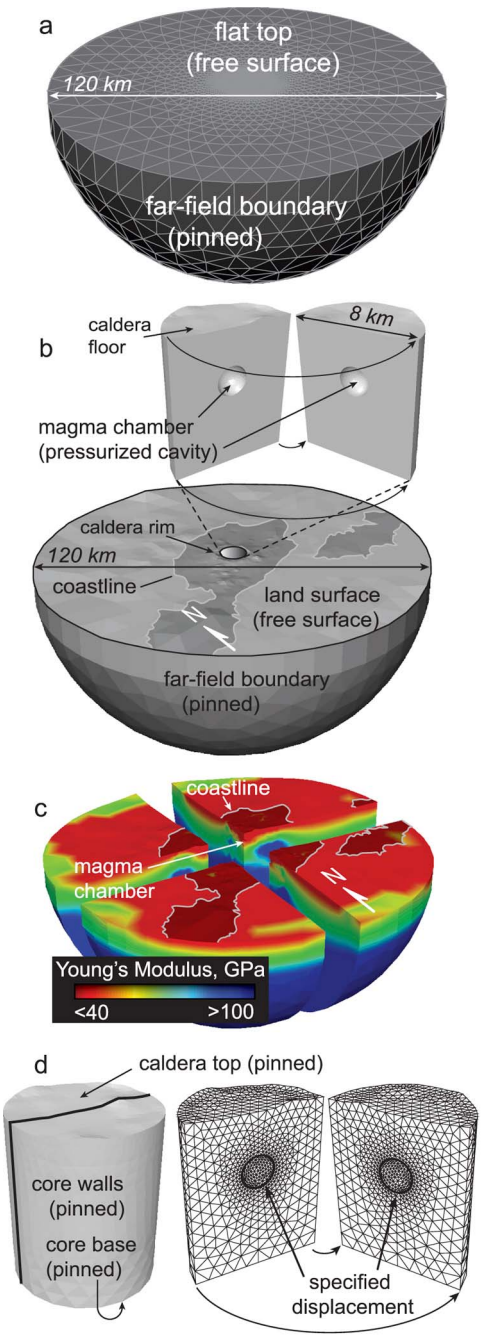


**Figure 2.** Domain configurations, as summarized in Table 2. (a) VAL. The model domain is a solid hemisphere with a diameter of 120 km. The flat top of the domain is a free surface. The curved lateral and depth boundary conditions are set to zero displacement (pinned). A pressure load is applied to an internal spherical cavity. This configuration is designed to simulate *Mogi* [1958]. (b) Configuration common to HET and HOM. Onshore regions are shaded darker than offshore regions and outlined with the coastline for reference. The exploded view of the subcaldera core reveals the initial estimated position of the magma chamber. (c) Three-dimensional distribution of material properties, shown in exploded view. Onshore regions are shaded darker than offshore regions and outlined with the coastline for reference. (d) CORE. (left) The outer surfaces of the domain have pinned boundary conditions. (right) An exploded view of the domain reveals the magma chamber and mesh. The nodes comprising the chamber have specified displacements.

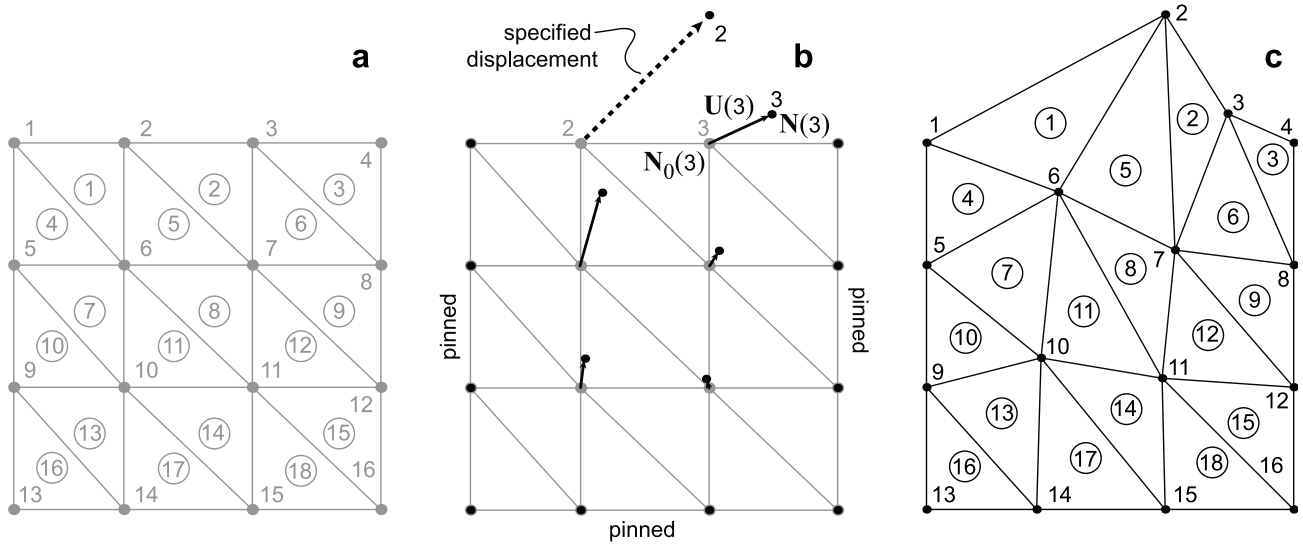


**Figure 3.** Pinned mesh perturbation (PMP). This two-dimensional schematic illustrates the principles of PMP. (a) Initial FEM mesh. The gray mesh is part of an FEM that simulates elastic plane strain. Filled gray circles are nodes with corresponding numeric names. Each element has a numeric name, shown here as a circled number. The geometry of each triangular element is defined by the position coordinates of three nodes. (b) Mesh perturbation. The mesh deforms in response to a specified displacement (dashed vector) applied to node 2 and zero displacement (pinned) boundary conditions along the sides and bottom of the domain. This deformation satisfies equation (1). Gray circles are initial nodal positions ($\mathbf{N}_0$). Black circles are final nodal positions ($\mathbf{N}$). Black arrows are design vectors ($\mathbf{U}$) that specify alterations to nodal positions over the mesh. An example of the relationship among the initial and final nodal positions and the design vector is labeled for node 3. (c) Final mesh. The distortion caused by the specified displacement of node 2 is distributed throughout the mesh. Element definitions, given as n-tuples of node names, are preserved, although the node positions may vary. This preservation of element definitions, while simultaneously allowing for element distortions, is the essence of PMP.

boundary, distortion is undesirably focused near the chamber. One way to better distribute the distortion throughout the core is to specify a series of shells surrounding the chamber, where the shells near the chamber are relatively stiff. From a mechanical standpoint, this configuration reduces the effective curvature of the spherical magma chamber and smoothes the mesh distortion resulting from perturbing the position of the magma chamber. More specifically, the Young's modulus, $E$, decreases linearly from a maximum, $E_1$, in the shell surrounding the magma to a minimum, $E_0$, for the elements furthest from the magma chamber (Figure 4).

[24] All FEMs presented here are comprised of first-order tetrahedral elements. Each tetrahedral element is defined by four nodes that occupy the vertices and are connected by six sides. A tetrahedral quality criterion, $q$, measures the deviation from an ideal regular tetrahedron:

$$q = q * V_T \left( \sum_{i=1}^{6} l_i^2 \right)^{-1.5} \tag{3}$$

where $q^*$ normalizes the quality criterion to range from 0 (poor) to 1.0 (regular tetrahedron), $V_T$ is the volume of the tetrahedron, and $l$ is the length of a tetrahedral edge [*Zuo et al.*, 2005; *Press et al.*, 2007]. This particular formulation for tetrahedron quality is both robust and computationally inexpensive [*Parthasarathy et al.*, 1994]. We use the PMP method to simulate the maximum range of allowable perturbations to the position of the chamber and evaluate the distortion of the tetrahedra as a function of $E_1/E_0$ (Figure 5). The distortion is minimized for $E_1/E_0 > 20$ and we use $E_1/E_0 = 100$ for the remainder of this analysis. That is, the elements closest to the magma chamber have a stiffness that is 100 times greater than the stiffness of elements furthest from the magma chamber and the variation between these limits is linear. To be clear, this configuration applies only to CORE, which perturbs the magma chamber position via PMP. While the resulting mesh (without material properties) from CORE is inserted into HET, the material properties for this inserted mesh are determined for HET as described below.

[25] Because we are simulating an elastic deformational system, each element in the model domain requires specifications for two elastic moduli. We use Young's modulus and Poisson's ratio out of convenience, because these are the two parameters that Abaqus requires for each elastic element. The relationship between Young's modulus and shear wave velocity, $V_s$, is:

$$E = 2\rho(1 + \upsilon) V_s^2 \tag{4}$$

where $\rho$ is density [*Jaeger et al.*, 2007]. This relationship between the static $E$ and dynamic $V_s$ is valid for depths greater than a few kilometers [*Simmons and Brace*, 1965].

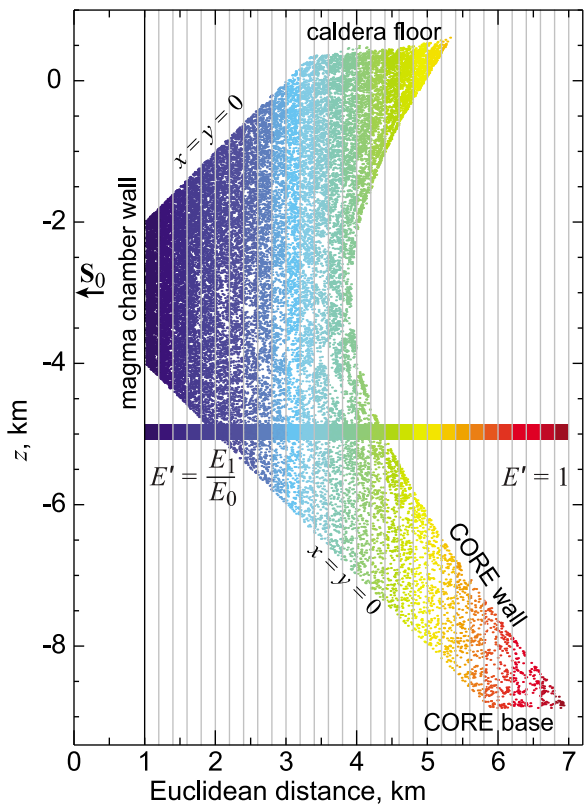


**Figure 4.** Stiffness shells for CORE. The gray vertical bars delimit the 30 stiffness shells. The color bar shows how the relative Young's modulus for each shell decreases linearly from $E' = E_1/E_0$ to unity. Each colored dot represents the position of an element's centroid with respect to the initial estimate of the magma chamber, $\mathbf{S}_0$. The colors correspond to the distribution of the relative Young's modulus.

Because $V_s$ is squared, variations in $V_s$ will dominate over other variables that contribute to estimations of $E$. We assume constant representative values of $\nu$ and $\rho$ for oceanic crust, where $\upsilon = 0.29$ and $\rho = 2900$ kg/m$^3$, for the bulk of the domain [*Christensen and Mooney*, 1995; *Christensen*, 1996]. The shallow LVZ within the caldera includes specifications $\upsilon = 0.15$ and $\rho = 2400$, to account for the relatively weak and fluid-saturated materials [*Wang*, 2000] suggested by previous studies [*Johnson et al.*, 2010; *Larsen et al.*, 2009; *Lu et al.*, 2005; *Masterlark*, 2007; *Masterlark et al.*, 2010].

[26] We specify values for $E$ over the model domain based on the $V_s$ model derived from ANT for Okmok (Figure 1b) [*Masterlark et al.*, 2010] using Laplacian interpolation [*Press et al.*, 2007]. First, we convert $V_s$ to $E$ using equation (4). Then, we construct an auxiliary FEM (Table 2), to satisfy the Laplacian $\nabla^2 E = 0$ using the same (unperturbed) mesh from HET. We assign values for $E$ to a subset of nodes (internal boundary conditions), according to the nearest-neighbor analysis of the $E$ distribution converted from the $V_s$ tomography model. Far-field boundary conditions for $E$ are specified according to the distribution converted from the initial layered $V_s$ structure [*Masterlark et al.*, 2010]. The auxiliary FEM then solves the Laplace equation for $E$ over the model domain and we extract the solution for element centroid positions. This produces a distribution of $E$ that precisely corresponds to the element centroid positions in the mesh of HET (Figure 2c). It is trivial to transfer the material properties determined with the auxiliary FEM to HET, because the meshes defined for both of these models are identical. HET is now configured to simulate a pressurized sphere embedded in a model domain having a distribution of material properties estimated from ANT and a free surface having the irregular geometry of topographic and bathymetric relief. We recognize that the tomography models have uncertainties that will propagate through the interpolation described above and into HET. However, a detailed analysis of how these uncertainties manifest themselves is far beyond the scope of this study. An additional model, HOM (Table 2), is defined by duplicating HET and replacing the distribution of material properties with a single pair of elastic moduli for the entire model domain (Table 2). A comparison of results from HET and

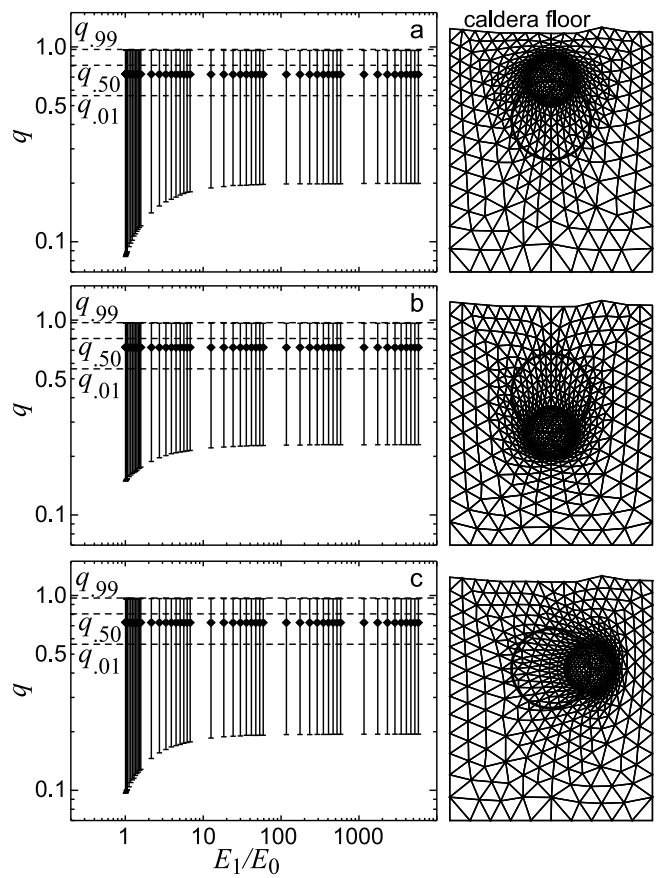


**Figure 5.** Maximum shell stiffness and tetrahedra quality for perturbation limits. The tetrahedra quality, $q$, range is 0 (poor) $\leq q \leq 1$ (regular tetrahedra), as defined by equation (4). Error bars denote 1st and 99th percentiles and the black diamonds are the median values. Dashed lines represent corresponding values for an unperturbed mesh. Mesh perturbations are shown at the right for $E' = E_0/E_1 = 100$. Heavy black circles denote the bounds constraining the search over the maximum parameter space for $\mathbf{S}$. (a) $\mathbf{S} = [0, 0, -1500$ m]. (b) $\mathbf{S} = [0, 0, -4500$ m]. (c) $\mathbf{S} = [1500$ m, 0, 0]. The improvement in perturbed mesh quality saturates for $E' = E_1/E_0 > 20$.

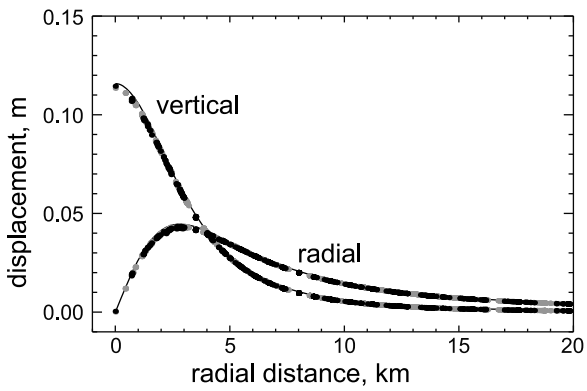


**Figure 6.** FEM validation. Solid lines are radial and vertical components of displacement for source depth of 4000 m [*Mogi*, 1958]. Black and gray circles are corresponding predictions calculated using VAL for coarse and fine mesh configurations, respectively.

HOM quantifies prediction sensitivities to variations in material properties.

#### 2.1.3. Validation

[27] Validation is a fundamental step in the modeling process to ensure that a numerical model is working properly [*Wang and Anderson*, 1982]. We can validate the FEM configuration by comparison of model predictions to known benchmarks, which ideally come from exact analytical solutions. Analytical solutions for displacement due to a pressurized spherical cavity embedded in an elastic domain having an irregular free surface and arbitrary distribution of material properties do not exist. It is for this reason that we turn to FEMs in the first place. We can, however, construct a simple FEM configuration called VAL having a pressurized spherical cavity embedded in homogeneous, hemispherical elastic domain with a planar, horizontal free surface (Table 2). The general domain geometry, loading conditions, and boundary conditions of VAL are not too different from its more sophisticated counterparts, HET and HOM (Figure 2). Because VAL well approximates the configuration of analytical HEHS *Mogi* [1958] models, we can compare predictions from VAL with results of analytical solutions to test the performance of the VAL configuration assemblage, as well as the validity of various mesh configurations.

[28] Expressed in index notation, as defined in the context of equation (1), the displacement for a given point on the free surface, caused by a pressurized sphere embedded in a homogeneous, isotropic elastic half-space, is:

$$u_i = C\,\frac{(x_i - S_i)}{D^3} \quad \text{with} \quad C = \Delta P(1-\nu)\frac{r_S^3}{G} = \Delta V\,\frac{(1-\nu)}{\pi} \tag{5}$$

where $C$ is the source strength, $\mathbf{S} = [S_x, S_y, S_z]$ is the position of the center of the spherical source, $D$ is the Euclidean distance from $\mathbf{S}$ to the point on the free surface, and $\Delta V$, $\Delta P$, and $r_S$ are the change in volume, the change in pressure, and the radius, respectively, of the embedded sphere [*Segall*, 2010]. We substitute an effective radius, $r_{Seff}$, for the embedded chamber in our calculations, because the FEM approximation of the volume of the embedded sphere is less than its analytical counterpart. Corresponding residuals from VAL are less than 5% for both coarse and fine mesh configurations (Figure 6). Because the coarse mesh configuration of VAL has a distribution of characteristic element lengths that is similar to the mesh of HET, the meshes of HET and HOM are validated.

### 2.2. Optimization

[29] We assume that the net line-of-sight displacement, $\tilde{u}$, for the $i$th InSAR pixel is a linear combination of contributions from the pressurized magma chamber, plane-shift, and noise:

$$\tilde{u}_i = P_s \hat{\mathbf{u}}_i \mathbf{L}^{\mathrm{T}} + p_1 x_i + p_2 y_i + p_3 \tag{6}$$

where $P_s$ is the scaling pressure, with $\Delta P = P_s\,\Delta P_0$; $p_1$, $p_2$, and $p_3$ are the coefficients of a plane to account for the displacement at an arbitrary reference location and horizontal components of the range gradients attributed to mismodeled orbital effects [*Massonnet and Feigl*, 1998]; and the superscript 'T' denotes the matrix transpose operator. The matrix $\hat{\mathbf{u}}$ is the displacement generated by $\Delta P_0$ applied to the magma chamber, as calculated with an FEM, and depends on $\mathbf{S}$ in a nonlinear fashion. Row $i$ of $\hat{\mathbf{u}}$ is a three-component vector of predicted displacements for position $i$. This formulation has $M = 4$ linear parameters and $N = 115{,}550$ InSAR pixels. The forward model and matrix expression of equation (6) for a given $\mathbf{S}$ is:

$$\mathbf{Gm} = \mathbf{d} = \left[\hat{\mathbf{u}}\ \mathbf{L}^{\mathrm{T}},\ \mathbf{x},\ \mathbf{y},\ \mathbf{1}\right]\left[P_s,\ p_1,\ p_2,\ p_3\right]^{\mathrm{T}} \tag{7}$$

where $\mathbf{G}$ is a matrix of Green's functions; $\mathbf{m}$ is the parameter vector; $\mathbf{e}$ is the residual; $\mathbf{d}$ is a column vector of the InSAR data, having corresponding pixel locations given by column vectors $\mathbf{x}$ and $\mathbf{y}$; and $\mathbf{1}$ is a column vector with all elements equal to unity.

[30] We combine nested Monte Carlo [*Press et al.*, 2007] and randomly iterated search [*Shirzaei and Walter*, 2007] methods to ensure quick convergence to robust parameter estimates. The algorithm linearizes the problem by randomly sampling the three-dimensional parameter space for $\mathbf{S}$ and solves for linear parameters $\boldsymbol{P}_s$, $p_1$, $p_2$, and $p_3$ for each realization of $\mathbf{S}$. The least squares linear inverse solution for equation (7) is $\mathbf{m}_{est} = [\mathbf{G}^{\mathrm{T}}\mathbf{G}]^{-1}\mathbf{G}^{\mathrm{T}}\mathbf{d}$, where $\mathbf{e} = [\mathbf{d} - \tilde{\mathbf{u}}]$ and $\tilde{\mathbf{u}} = \mathbf{G}\ \mathbf{m}_{est}$ [*Menke*, 1989]. Best fit solutions are achieved by adaptively decreasing nested parameter bounds for $\mathbf{S}$, until all seven calibration parameters converge. A detailed description of the nested Monte Carlo procedure follows.

[31] First, we specify initial bounds on the three-dimensional parameter space for $\mathbf{S}$. These bounds form the surface of a sphere (not to be confused with the spherical magma chamber), for which the two horizontal coordinates have been estimated using an HEHS model [*Masterlark*, 2007]. Previous studies indicate that this position is robust for HEHS models [*Masterlark et al.*, 2010, and references therein]. The initial depth estimate is a compromise between the shallower expected depths from HEHS models ($-3000$ m $< S_z < -2000$ m) and deeper source positions ($S_z = -4000$ m) expected from tomography models [*Masterlark et al.*, 2010] and the influence of weak materials in the shallow caldera [*Masterlark*, 2007]. The initial estimate of the sphere's position is $\mathbf{S} = \mathbf{S}_0 = [0, 0, -3000\ \mathrm{m}]$ and the initial radius of the bounding sphere is 1500 m, effectively constraining the solution for $\mathbf{S}$. Second, we specify an adaptation schedule for the radius $b$ of the bounding sphere.

**Table 3.** Calibrated Parameters[a]

| | HET | HET Recovery Test | HOM |
|---|---|---|---|
| $S_x$[b] (m) | $-18^{+52}_{-52}$ | $-18$ | $40^{+50}_{-49}$ |
| $S_y$[b] (m) | $-71^{+63}_{-58}$ | 71 | $83^{+64}_{-64}$ |
| $S_z$[b] (m) | $-3527^{+55}_{-54}$ | $-3527$ | $-2665^{+42}_{-46}$ |
| $\Delta P$ (MPa) | $-328^{+12}_{-12}$ | $-328$ | $-361^{+13}_{-12}$ |
| $\Delta V \times 10^7$ (m$^3$) | $-6.1$ | $-6.1$ | $-5.4$ |
| $p_1 \times 10^{-7}$ | $3.81^{+0.21}_{-0.22}$ | 3.82 | $4.70^{+0.24}_{-0.23}$ |
| $p_2 \times 10^{-8}$ | $-3.92^{+1.45}_{-1.36}$ | $-3.93$ | $-2.23^{+1.39}_{-1.42}$ |
| $p_3 \times 10^{-2}$ (m) | $-5.11^{+0.18}_{-0.18}$ | $-5.11$ | $-4.46^{+0.20}_{-0.19}$ |
| $\mathbf{e}^T\mathbf{e}$ (m$^2$) | 16.506 | $1.78 \times 10^{-4}$ | 16.929 |
| Signal recovery | 92.9% | | 92.7% |
| Linear parameters ($M$) | 4 | | 4 |
| $\nu$ ($M - N$) | 115,546 | | 115,546 |
| $R^2_{xy}$ | 0.01 | | 0.15 |
| $R^2_{xz}$ | 0.18 | | 0.18 |
| $R^2_{yz}$ | 0.19 | | 0.19 |
| $R^2_{z\Delta P}$ | 0.82 | | 0.78 |

[a]Reported uncertainties are 2.5% and 97.5% quantiles.
[b]With respect to the origin defined in Table 2.

This schedule includes a total of 12 adaptations for the parameter bounds that begin with $b_0$ = 1500 m and incrementally decrese to $b_{11} \sim 6$ m:

$$b_t = b_0 \ e^{-t/2} \tag{8}$$

where $t$ is a vector of increasing integers spanning $0 \le t \le 11$. The radius of the spherical parameter space for all adaptations is described by the vector $\mathbf{b} = [b_0 \ldots b_{11}]$. For each adaptation, the random realizations of $\mathbf{S}$ are constrained by the union of spheres having $b_t$ centered on $\mathbf{S}_t$ and $b_0$ centered on $\mathbf{S}_0$. This adaptation schedule provides a good compromise between quick convergence and resistance to local minima, as presented later in the results section. Third, we implement the nested Monte Carlo method to search for optimal solutions for sequentially decreasing parameter bounds for $\mathbf{S}$. Beginning with the initial parameter bounds ($b_0$ centered on $\mathbf{S}_0$), the procedure specifies 100 random realizations of $\mathbf{S}$. Displacements ($\hat{\mathbf{u}}$) are calculated for each realization using the PMP method and $\Delta P$, $p_1$, $p_2$, and $p_3$ are estimated with the least squares inverse method [*Menke*, 1989]. The best solution is identified and the initial position $\mathbf{S}_0$ is updated to $\mathbf{S}_1$ according to corresponding parameters of the best solution. The procedure thus adapts to new spherical bounds ($b_1$ centered on $\mathbf{S}_1$) for $\mathbf{S}$ and the process is repeated. This procedure continues through 12 adaptations, after which the solution has converged to a position precision of about 6 m. Finally, we conduct this process 10 times, each having a new randomization seed, to ensure robust convergence to a global solution. Ultimately, the procedure samples 12,000 random realizations of the three-dimensional nonlinear parameter space for $\mathbf{S}$. Once we specify the initial bounds and the adaptation schedule, the procedure is fully automated. We conduct the entire optimization process and post processing, other than FEM execution, with IDL (version 6.4, ITT Visual Information Solutions, Boulder, Colorado, 2007) software.

## 3. Results and Discussion

[32] Each realization of $\mathbf{S}$ and corresponding estimates for $\Delta P$, $p_1$, $p_2$, and $p_3$ takes about 47 s using parallel computation on three cores of a 3 GHz quad core CPU with sufficient physical memory to contain the entire equation solver, thus minimizing computationally expensive input/output operations. The total analysis time for 24,000 realizations (12,000 each for HET and HOM) is about 14 days. The results are summarized in Table 3. Estimates of the source parameters for both configurations converged to a solution by adaptation $t$ = 7 for all randomly iterated searches (Figure 7).

[33] The misfit determined from the summed square of residuals HET, calculated using the best fitting estimate of the model parameters, is $\mathbf{e}^T\mathbf{e}$ = 16.51 m$^2$. The corresponding misfit value for HOM is slightly larger, $\mathbf{e}^T\mathbf{e}$ = 16.93 m$^2$. From the misfit for HET, we determine the a posteriori uncertainty of a single InSAR measurement to be $s = [\mathbf{e}^T\mathbf{e}/(N - M)]^{1/2}$ = 12.0 mm. The preceding calculation, however, neglects the correlations between InSAR pixels, rendering subsequent goodness-of-fit tests problematic [e.g., *Aster et al.*, 2005; *Lohman and Simons*, 2005]. Nonetheless, we can compare HET to HOM. To do so, we test the null hypothesis that the HOM and HET residuals sample normal

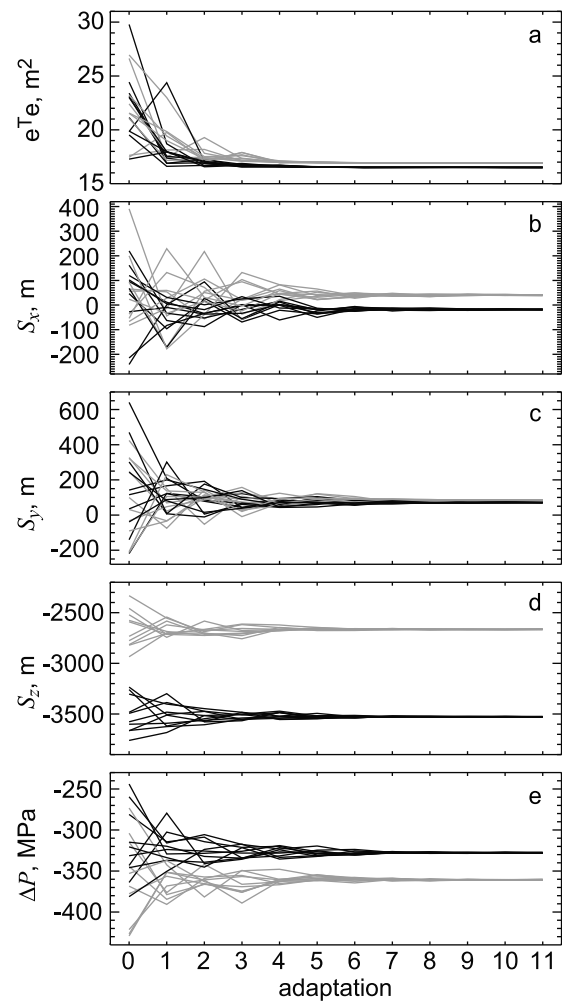


**Figure 7.** Convergence of calibration parameter estimates. Black and gray curves are from HET and HOM, respectively. Convergence is achieved by adaptation $t$ = 7 ($b_7$ = 45 m) for all calibration parameters. (a) Misfit, $\mathbf{e}^T\mathbf{e}$. (b) $S_x$. (c) $S_y$. (d) $S_z$. (e) $\Delta P$.

distributions with the same variance, such that $H_0$: $s^2_{HOM} = s^2_{HET}$ using an F test [*Larsen and Marx*, 1986; *Menke*, 1989]:

$$\mathrm{F} = \frac{s_1^2}{s_0^2} \quad \text{with} \quad s^2 = \frac{1}{N-1}\sum_{i=1}^{N} e_i^2 \tag{9}$$

In this case, $S_0^2 = S^2_{HET}$ and $S_1^2 = S^2_{HOM}$. The value of the test statistic is F = 16.93/16.51 = 1.03. Since the number of degrees of freedom is $\nu = N - M = 115{,}550 - 4$ for both configurations, the critical value for a significance level of $\alpha = 0.05$ is $\mathrm{F}(1 - \alpha/2, \nu, \nu) = 1.01$. Thus, the null hypothesis is rejected with 95% confidence. We conclude that displacement predictions from HET fit the observed values (as measured by InSAR) significantly better than those predicted with HOM.

[34] We conduct a recovery test to validate the PMP-based nested Monte Carlo method. First, we calculate $\tilde{\mathbf{u}}$ from HET and the corresponding best fit parameter values, $\mathbf{m}_{est}$. Then, we execute 10 randomly iterated searches using the nested Monte Carlo optimization scheme specified above for HET and treat $\tilde{\mathbf{u}}$ as the data vector. The misfit for this recovery test is $\mathbf{e}^{\mathrm{T}}\mathbf{e} = 1.78 \times 10^{-4}$ m$^2$, with a root-mean squared error of $4.0 \times 10^{-5}$ m. The 95% confidence interval for each estimated parameter includes the value used to generate the synthetic deformation field, thus validating the PMP-based nested Monte Carlo method.

[35] Now that we have validated our estimation method, we use the results from these two best fitting configurations for HET and HOM as the basis to determine acceptable alternatives from the 12,000 respective realizations of **S**. In this case, the null hypothesis is $H_0$: Predictions of the best fit model are equivalent to predictions from alternative models that simulate different realizations from **S**. The alternative hypothesis is $H_\mathrm{A}$: Predictions of the best fit model are better than predictions from alternative models that simulate different realizations from **S**. We conduct a series of F tests comparing the best fit model to models having different realizations of **S** and determine acceptable realizations of **S**. This analysis is performed separately for HET and HOM using equation (9). In this case, we calculate $s_0^2$ from the best fit model and $s_1^2$ for each of the 12,000 alternative realizations. Again, the critical value for a significance level of 0.05 is 1.01. We reject the null hypothesis for many of the alternative models. The distribution of estimates for which the null hypothesis is not rejected delimits the region of 95%

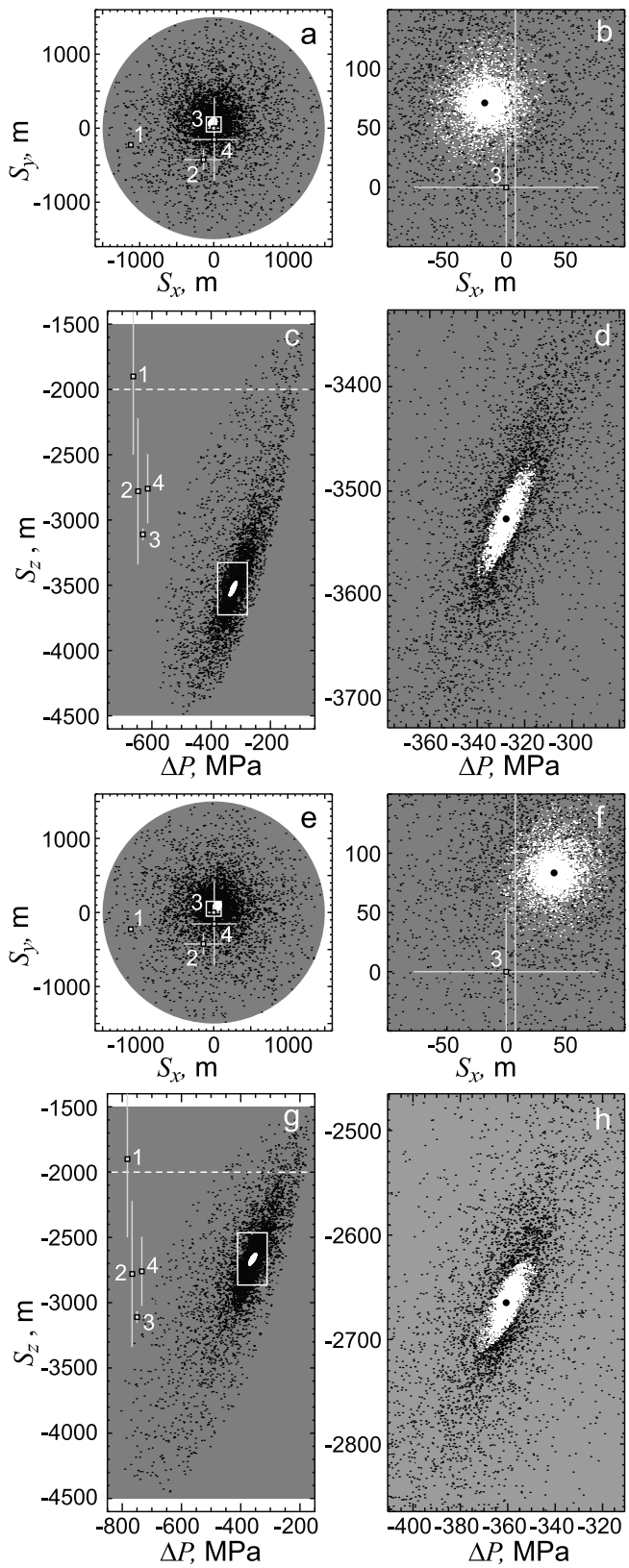


**Figure 8.** Distributions of parameter estimates from pairwise cross sections of the parameter space. Black dots are samples from the nested Monte Carlo parameter space. White dots include the 95% confidence regions for estimated parameters. Black circles are best estimates. Selected results (black squares with $\pm 2\sigma$ uncertainties) from prior studies are superposed for reference: 1, *Lu and Dzurisin* [2010] (first 13 h of 2008 eruption, uncertainties not reported for horizontal position); 2, *Lu et al.* [2010] (1997–2008 inter-eruption); 3, *Masterlark et al.* [2010] (1997 eruption); and 4, *Lu et al.* [2005] (1997 eruption). (a–d) Results for HET. (e–h) Results for HOM. Figures 8a and 8e show horizontal position of source. Figures 8b and 8f are the respective insets from Figures 8a and 8e. Figures 8c and 8g show depth versus change in pressure. White dashed line denotes location of VLP tremor source [*Haney*, 2010]. Light gray regions represent petrologic depth constraints [*Izbekov et al.*, 2005]. Estimates of pressure changes, which are strongly dependent on an assumed radius for the magma chamber, are not shown for prior results. Figures 8d and 8h are the respective insets from Figures 8c and 8g.

confidence in the parameter space (Figure 8). Reported uncertainties in Table 3 are 2.5% and 97.5% quantiles for each parameter.

[36] The estimated horizontal position is not sensitive to the three-dimensional distribution of material properties for Okmok volcano (Figure 8). Results from HET, HOM, and previous HEHS-based studies that estimated the horizontal position of the deformation source of the 1997 eruption of Okmok [e.g., *Lu et al.*, 2005; *Masterlark et al.*, 2010] are similar (Figure 8). We calculate Pearson's linear correlation coefficient ($R$) to characterize the linear association among the source position parameters for each of the acceptable models:

$$R_{ij}|_{i\neq j} = \frac{\sum_m \left(S_{i,m} - \bar{S}_i\right)\left(S_{j,m} - \bar{S}_j\right)}{\sqrt{\sum_m \left(S_{i,m} - \bar{S}_i\right)^2}\sqrt{\sum_m \left(S_{j,m} - \bar{S}_j\right)^2}} \tag{10}$$

where $m$ is an index for acceptable estimates identified with F tests, $i$ and $j$ are coordinate indices, and $\bar{S}$ is the mean [*Press et al.*, 2007]. These calculations are performed separately for results from HET and HOM and summarized in Table 3. Linear correlation coefficients for all three parameters describing the position of the source are less than 0.2 for both HET and HOM. In particular, linear correlation coefficients of $R^2_{xy} = 0.10$ and $R^2_{xy} = 0.15$ indicate that the two estimated horizontal position components are weakly correlated for both HET and HOM, respectively, in agreement with results from previous analyses of the 1997 eruption of Okmok [*Lu et al.*, 2005; *Masterlark et al.*, 2010]. For the case of Okmok, an HEHS model without standard topographic corrections [e.g., *Williams and Wadge*, 1998] is sufficient to estimate the horizontal location of a spherical pressure source. This is a particularly useful result, because HEHS analyses are computationally inexpensive compared to FEM-based counterparts. Therefore, the dimensions of the parameter space may be reduced by two by treating the two horizontal position components of the spherical deformation source as constraining information, rather than calibration parameters. This simplification corresponds to a two-thirds reduction in the total computation time for the inversions. For the specific case of the 1997 eruption of Okmok volcano, the combination of fewer nested Monte Carlo adaptations and a fixed horizontal position of the deformation source would reduce the total computation time to less than 3 days for HET.

[37] In contrast, the estimated depth of the source is sensitive to the specific distribution of material properties (Figures 7 and 8). The estimated vertical source positions for HET and HOM are $S_z = -3527^{+55}_{-54}$ m and $S_z = -2665^{+42}_{-46}$ m, respectively. In particular, the relatively weak materials that fill the shallow caldera strongly influence the estimated depth of the deformation source by focusing the deformation within the caldera. This effect allows deeper deformation sources to produce a pronounced peak of deformation within the caldera that combines with a longer wavelength of deformation on the volcano's flanks. This deformation pattern is challenging to distinguish from that of a shallower deformation source embedded in a HEHS, as pointed out in a previous study [*Masterlark*, 2007]. While HET, HOM, and previous HEHS-based models all fit the deformation data reasonably well, the presence of the weak zone leads to a deeper deformation source that is consistent with the deep LVZ of tomography models [*Masterlark et al.*, 2010]. Petrologic studies of the 1997 Okmok lava suggest $-3700$ m $< S_z < -2900$ m [*Izbekov et al.*, 2005], which supports the deeper deformation source estimated for HET. *Dieterich and Decker* [1975] describe an experiment where a borehole was drilled in Kilauea caldera to confirm the position of a spherical magma chamber predicted from deformation data [*Kinoshita et al.*, 1969]. When borehole temperature measurements failed to detect a magma chamber at the predicted position, *Dieterich and Decker* [1975] suggested that a non-spherical shape of the chamber was responsible. Here, we suggest an alternative explanation. Attempting to simulate a heterogeneous distribution of material properties with an HEHS model predicts an apparent source depth that is systematically too shallow.

[38] The estimated change in pressure for both HET and HOM is $\Delta P = \sim 350$ MPa (Figures 7 and 8), corresponding to changes in volume of $\Delta V = 0.06$ km$^3$ and $\Delta V = 0.05$ km$^3$, respectively. The observed volume of lava erupted in 1997 is $0.154 \pm 0.025$ km$^3$. Assuming 25–75% vesicularity [*Lu et al.*, 2003], we find the dense rock equivalent volume to be between 0.03 and 0.13 km$^3$. Predictions from both models are in excellent agreement with the volume of lava inferred independently [*Lu et al.*, 2003]. Therefore, both the HET and HOM configurations are verified. Interpretations of the estimated changes in pressure, which depend on the assumed magma chamber radius of 1000 m, are problematic because they greatly exceed lithostatic conditions and the tensile strength of rock ($\sim$10 MPa [*Jaeger*, 1956]) for the estimated deformation source depths. However, equation (5) indicates that the estimated change in pressure is proportional to the cube of the magma chamber radius and we can arbitrarily reduce the estimated change in pressure by increasing the assumed radius of the magma chamber.

[39] Studies of very long period (VLP) tremor suggest that the 2008 eruption of Okmok was fed by fluids exiting the magma chamber into a shallow crack-like conduit at $z = -2000$ m [*Haney*, 2010]. HEHS-based studies of InSAR data for the 2008 eruption, the 1997–2008 inter-eruption period, and the 1997 eruption confirm that the vertical position of the deformation source, $-3000 < S_z < -2000$ m, is generally persistent [*Lu et al.*, 2003, 2005; *Lu and Dzurisin*, 2010; *Lu et al.*, 2010; *Mann et al.*, 2002; *Masterlark*, 2007; *Masterlark et al.*, 2010]. On the other hand, *Freymueller and Kaufman* [2010] suggest that the vertical source position may be shallower for the 2008 eruption than for the 1997 eruption. Results from HOM (the HEHS approximation) in this study are generally consistent with these previous results (Figures 7 and 8). If we assume that the magma chamber is a pressurized spherical cavity (rather than some assembly of deformation sources that effectively behaves as a pressurized sphere) and assume that the source position is stationary in time, we can combine the VLP-based tremor source location of $z = -2000$ m from the 2008 eruption and maximum hoop stress to graphically estimate the radius of the magma chamber corresponding to HET and HOM (Figure 9). The maximum hoop stress for a pressurized sphere embedded in an HEHS occurs along the latitude of the sphere that is tangent to a cone having an apex that intersects the free surface and is horizontally centered

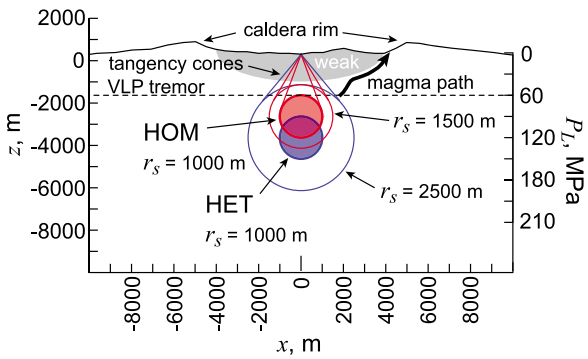


**Figure 9.** Schematic comparison of pressure estimates. The lithostatic pressure ($P_L$) is approximated using $P_L = -\rho g z$, where $\rho$ = 3000 kg/m$^3$, $g$ = 10 m/s$^2$, and $z$ is the depth beneath the caldera floor. The assumed density represents an upper limit. Lower densities would decrease the lithostatic pressure and thus decrease the allowable change in pressure within the magma chamber. Blue and red circles represent spherical magma chambers for HET and HOM, respectively. Dike breakout occurs at the spherical latitude where the cone is tangent to the corresponding sphere [*McTigue*, 1987] and corresponds to the depth of the very long period (VLP) tremor [*Haney*, 2010]. The gray region represents the weak materials filling the shallow caldera. The thick black arrow represents the path of magma migration, which follows the base of the weak materials and intersects the caldera floor near the rim of the caldera [*Masterlark et al.*, 2010].

over the sphere [*McTigue*, 1987]. Assuming this latitude of maximum hoop stress corresponds to the VLP tremor source, we find a magma chamber radius for the HOM configuration of about 1500 m. This corresponds to a pressure change of $\Delta P$ = 107 MPa, which still exceeds lithostatic constraints. Using the same analysis, the magma chamber radius for HET should be about 2500 m and is substantially larger than that of HOM, because the center of the magma chamber for HET is much deeper. This larger chamber corresponds to a pressure change of $\Delta P$ = 21 MPa, which is well within lithostatic constraints for the entire depth range spanned by this magma chamber.

[40] Several studies suggest rheologic partitioning that includes a viscoelastic region surrounding the magma chamber can account for deformation, but require substantially lower pressure changes compared to purely elastic counterparts [*Del Negro et al.*, 2009; *Jellinek and DePaolo*, 2003; *Masterlark et al.*, 2010; *Newman et al.*, 2006]. During a finite time interval, deviatoric stresses in the viscoelastic material will relax via viscous flow in response to an applied stress. This viscoelastic relaxation in the region surrounding the chamber effectively increases the chamber size [*Segall*, 2010], thus increasing deformation while maintaining a constant pressure change. Although thermal models predict a viscoelastic rind surrounding active magma chambers [e.g., *Del Negro et al.*, 2009; *Masterlark et al.*, 2010], the inclusion of viscous flow, a transient process, would greatly increase computational requirements. Furthermore, adjustable viscous flow parameters would increase the dimension of the parameter space. This additional complexity is beyond the scope of this study.

[41] Near the center of the caldera and adjacent to the northern limit of the 1997 lava flow, the residual deformation field exhibits unexpected structure (Figure 10). Both HET and HOM over-predict subsidence near the caldera center and under-predict the subsidence on the flanks of the volcano. HEHS-based analyses indicate that a model with an ellipsoidal, rather than spherical, magma chamber does not significantly improve the fit to InSAR data spanning the inter-eruption interval between the 1997 and 2008 eruptions of Okmok [*Lu et al.*, 2010]. Therefore, if the position of the deformation source spanning the 1997 and 2008 eruption cycle is nearly stationary, as suggested by others [*Lu et al.*, 2005, 2010; *Lu and Dzurisin*, 2010], then the shape of the chamber is probably not the cause of the systematic misfit near the center of the caldera. Instead, this misfit is likely due to the local subsidence within the caldera caused by the surface loading of the lava flow [*Lu et al.*, 2005] that has not been accounted for in this study.

[42] A closer inspection of the residuals reveals the failure of a single deformation source model (depressurization of a magma chamber) to adequately satisfy our assumption that the residuals are a good estimate of the noise (Figure 11). The null hypothesis is $H_0$: The residuals are random noise. We construct normal quantile-quantile plots (Figures 11b and 11d) of the residuals to test this hypothesis [*Walpole et al.*, 2007]. The residuals have excessively heavy tails with 95% confidence that are incompatible with a Gaussian distribution and we reject the null hypothesis.

[43] As sketched in Figure 12, the residuals represent a deformation pattern caused by gravitational loading of the 1997 lava flow that is not accounted for in our models. We envision a future analysis of InSAR-observed deformation spanning the complete 1997–2008 eruption cycle, in an effort to investigate the transient behavior of magma migration and storage within Okmok volcano. Such an analysis will account for the gravitational loading of the 1997 lava flow to correct the systematic residuals discussed above, as well as simulate temperature-dependent rheological properties that allow for transient deformation [e.g., *Masterlark et al.*, 2010].

[44] The PMP method presents a simple solution to the problem of simulating geometric entities of arbitrary complexity, such as topography and bathymetry derived from DEMs. This method would work equally well for internal partitioning surfaces, such as boundaries between regions with different rheologic properties. In this study, we demonstrate the PMP method for a deformational system having a simple pressurized spherical cavity as the deformation source. In this case, there are three calibration parameters describing the position of the center of the pressurized sphere that must be estimated using nonlinear optimization. The methods are readily extended to pressurized cavities having more complicated geometric configurations, such as triaxial ellipsoids and planar dikes and sills, as well as elastic dislocations along faults [*Masterlark*, 2003]. One could design a deformational system having arbitrary deformation source shapes using spherical harmonics and calibration parameters for the corresponding coefficients. However, the dimension of the parameter space strongly controls the computational cost. Consequently, one must carefully design the nonlinear inverse analysis to

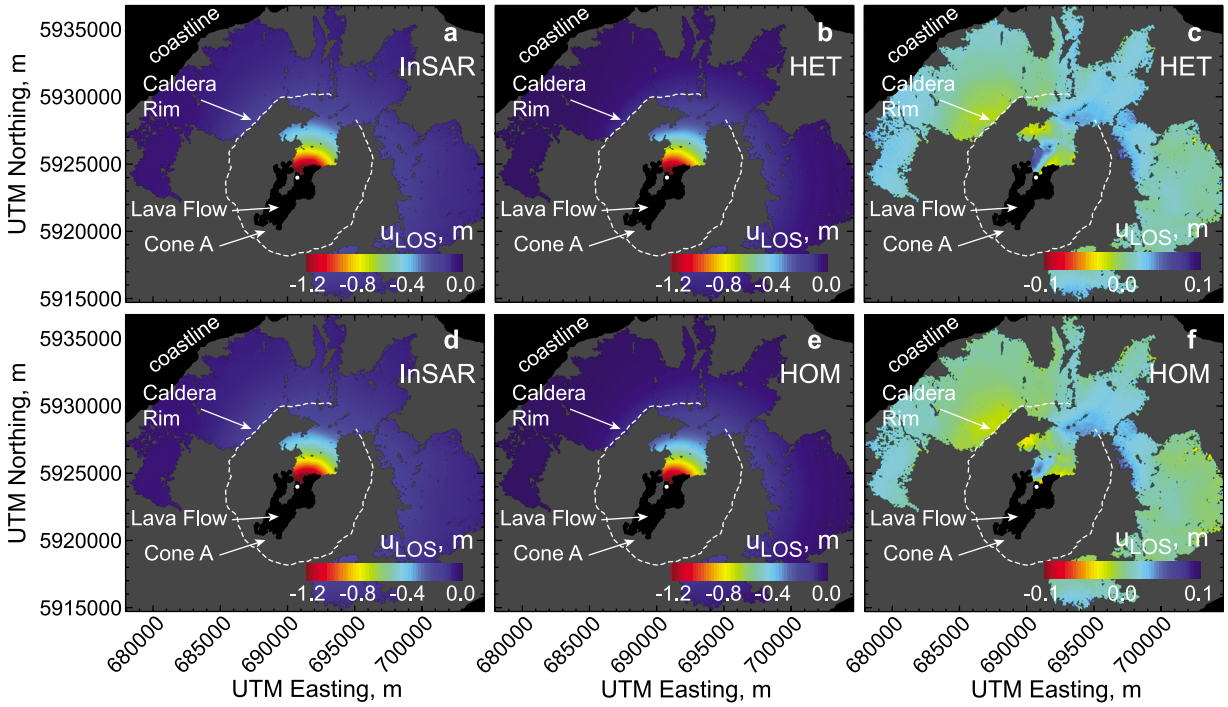


**Figure 10.** Predicted line-of-sight deformation. The white circle at center of the caldera is the horizontal position of $\mathbf{S}_0$. (a and d) InSAR data, duplicated from Figure 1 for ease of comparison. (b and e) Predicted InSAR for HET and HOM, respectively. (c and f) Residual for HET and HOM, respectively. Note the different deformation scale in the residual plots versus the InSAR and predicted plots. Blue and yellow residual regions indicate over-predicted and under-predicted subsidence, respectively.

account for computational limitations and ensure that the available data warrant the additional model complexity.

## 4. Conclusions

[45] The methods presented here allow us to combine nonlinear inverse methods with the capabilities of FEMs to simulate complex deformational systems having three-dimensional model domains and arbitrary geometric configurations and distributions of elastic material properties. More specifically, the FEM-based PMP method satisfies the primary objective of this study, which is to automatically impose geometric perturbations and re-meshing that are necessary to embed FEMs directly into iterative nonlinear optimization schemes. To the best of our knowledge, this is the first study to fully automate the calibration of nonlinear deformation source parameters using three-dimensional FEMs that simulate volcano deformation.

[46] The three-dimensional distribution of material properties simulated by the FEMs strongly influences some of the estimated nonlinear parameters. Horizontal position is not sensitive to the three-dimensional distribution of material properties for Okmok volcano. In this case, an HEHS model is sufficient to estimate the horizontal location of a spherical pressure source. However, the depth of the deformation source is sensitive to the presence of a shallow layer of weak materials filling the caldera. The estimated depths of the source are $3527^{+55}_{-54}$ m and $2665^{+42}_{-46}$ m below sea level for model domains simulating heterogeneous (HET) and homogeneous (HOM) distributions of material properties, respectively. The deeper source position is in accord with

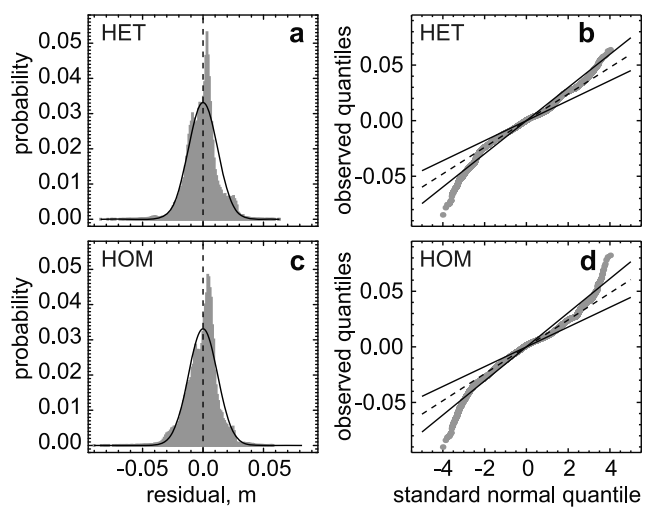


**Figure 11.** Best fit residual. (a and c) Probability density functions of residuals. Solid black curves and dashed vertical lines show theoretical distributions and associated mean values. (b and d) Normal quantile-quantile plot of residuals. Dashed lines are least squares estimates from linear regressions. Solid curves bound the 95% confidence for the mean response [*Walpole et al.*, 2007]. Departures from a straight line at both tails of the distribution indicate large residuals inside the caldera, near the lava flow (Figures 10c and 10f). These heavy tails, a result common to both HET and HOM, indicate that the single deformation source (pressurized spherical magma chamber) is insufficient to account for the InSAR observations in this region.

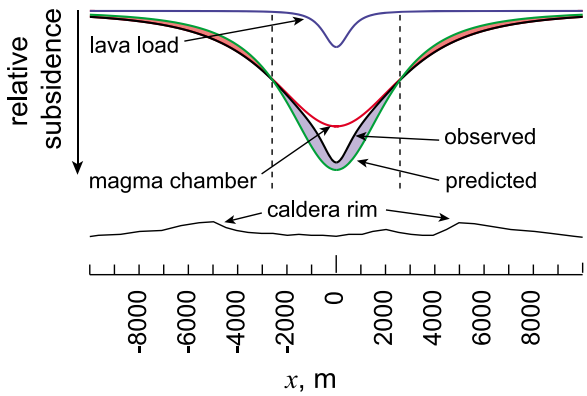


**Figure 12.** Schematic of gravitational loading effects. A west-east cross section of the volcano's elevation (VE = 1:1) is shown at the bottom for spatial reference. The observed deformation (black curve) is assumed to be purely vertical in this schematic and is the net response to localized gravitational loading of the lava flow (blue curve), and the volcano-wide deformation of magma chamber depressurization (red curve). The best fitting model (green curve) tries to simulate the net deformation with only a single volcano-wide deformation source and over-predicts subsidence in the central caldera (blue shaded region) and under-predicts subsidence elsewhere (red shaded region). This misfit pattern is evident in Figures 10c and 10f and explains the heavy tails in the normal quantile-quantile plot (Figures 11b and 11d).

available constraints from tomography models and petrology. Furthermore, a statistical test confirms that the fit of HET is a significant improvement at the 95% confidence level, compared to the fit of HOM.

[47] Because our analysis is limited to a purely elastic rheology and simulates magma chambers with a radius of 1000 m, the estimated changes in pressure exceed 300 MPa for both HET and HOM. These pressure changes exceed lithostatic pressure, although the corresponding changes in volume are consistent with the observed lava flow. VLP tremor observations and hoop stress arguments suggest that the radius of the magma chamber for HET is 2500 m, reducing the required change in pressure to 21 MPa, well within lithostatic constraints. These same arguments suggest that the radius of the magma chamber for HOM is 1500 m, which implies a pressure change of 107 MPa that still exceeds lithostatic constraints. The failure of an HEHS-based analysis to account for tomography models of Okmok volcano translates to underestimating the depth of the magma chamber and overestimating the pressure change within the magma chamber. HEHS models of Okmok volcano are useful for providing initial conditions for FEM-based nonlinear inverse analyses, but are unreliable for quantitative interpretations of magma migration and storage. We propose that future analyses of deformation for Okmok volcano include both forward and inverse models that account for petrologic constraints, the distribution of material properties available from tomography models, rheologic properties consistent with thermal models, and gravity loading due to lava emplacement. The FEM-based PMP methods presented here are sufficient to satisfy these requirements.

## Notation

$\mathbf{1}$ vector having all elements equal to unity.
$a$ index, dimensionless.
$b$ radius of sphere describing the parameter bounds, m.
$b_0$ initial radius of sphere describing the parameter bounds, m.
$\mathbf{b}$ vector of radii for parameter bounds, m.
$C$ source strength, $m^3$.
$\mathbf{d}$ vector of InSAR line-of-sight displacements, m.
$D$ Euclidean distance, m.
$e$ residual, m.
$\mathbf{e}$ vector of residuals, m.
$E$ Young's modulus, Pa.
$E'$ relative Young's modulus, dimensionless.
$g$ gravitational acceleration, $m/s^2$.
$G$ shear modulus, Pa.
$\mathbf{G}$ Green's functions, matrix.
$i$ index, dimensionless.
$j$ index, dimensionless.
$l$ length of tetrahedral edge, m.
$\mathbf{L}$ average line-of-sight, unit vector.
$m$ index, dimensionless.
$\mathbf{m}$ parameter vector.
$M$ number of parameters, dimensionless.
$\mathbf{N}$ nodal definition matrix.
$\mathbf{N}_0$ initial nodal definition matrix.
$N$ number of observations, dimensionless.
$p_1$ eastward component of range gradient, dimensionless.
$p_2$ northward component of range gradient, dimensionless.
$p_3$ additive range shift, m.
$P_L$ lithostatic pressure, Pa.
$\Delta P$ change in pressure, Pa.
$\Delta P_0$ impulse change in pressure, Pa.
$P_s$ pressure scaling coefficient, dimensionless.
$q$ normalized quality of tetrahedron, dimensionless.
$q^*$ normalizing coefficient, $m^{-3.5}$.
$r_S$ radius of magma chamber, m.
$r_{Seff}$ effective radius of magma chamber, m.
$R$ Pearson's linear correlation coefficient, dimensionless.
$s^2$ sample variance, $m^2$.
$S$ magma chamber position coordinate, m.
$\bar{S}$ mean of a magma chamber position coordinate, m.
$\mathbf{S}$ magma chamber position vector, m.
$\mathbf{S}_0$ initial magma chamber position vector, m.
$t$ index adaptations for parameter bounds, dimensionless.
$u$ displacement component, m.
$\mathbf{u}$ displacement vector, m.
$\hat{\mathbf{u}}$ matrix of displacements generated by impulse change in pressure, m.
$\tilde{\mathbf{u}}$ vector of net predicted displacements, m.
$\mathbf{U}$ domain design matrix.
$\Delta V$ change in volume of magma chamber, $m^3$.
$V_s$ shear wave velocity, m/s.
$V_T$ volume of tetrahedron, $m^3$.
$x$ Cartesian position component, m.
$\mathbf{x}$ Cartesian position vector, m.

$y$ Cartesian position component, m.
$\mathbf{y}$ Cartesian position vector, m.
$z$ Cartesian position component, m.
$\alpha$ level of statistical significance, dimensionless.
$\nu$ degrees of freedom, dimensionless.
$\rho$ density, kg/m$^3$.
$\upsilon$ Poisson's ratio, dimensionless.

[48] **Acknowledgments.** This work is supported in part by the U.S. Geological Survey Volcano Hazards Program/ARRA awards G10AC00018 and G10AC00039, NSF Geophysics EAR-0943943 and EAR-0943965, National Aeronautics and Space Administration (NASA) under award 10-Earth10F-0200, and a JAE-PREDOC grant from the CSIC. Academic licensing and technical support for Abaqus software is provided by Dassault Systèmes Simulia Corp. Paul Del Vecchio of Cray, Inc., provided excellent technical support for cluster computing. We thank Herbert F. Wang for helpful discussions regarding tensile strength and static versus dynamic rock properties. Insightful reviews by Tom Parsons (Associate Editor), Maurizio Battaglia, and Agust Gudmundsson greatly improved this paper.

## References

Aster, R. C., B. Borchers, and C. H. Thurber (2005), *Parameter Estimation and Inverse Problems*, 301 pp., Elsevier, San Diego, Calif.

Begét, J. E., J. F. Larsen, C. A. Neal, C. J. Nye, and J. R. Schaefer (2005), Preliminary volcano-hazard assessment for Okmok volcano, Umnak Island, Alaska, *DGGS Rep. of Invest., 2004-3*, 32 pp., Alaska Dep. of Nat. Resour., Anchorage.

Burgisser, A. (2005), Physical volcanology of the 2,050 BP caldera-forming eruption of Okmok volcano, Alaska, *Bull. Volcanol.*, *67*, 497–525, doi:10.1007/s00445-004-0391-5.

Caplan-Auerbach, J., S. Moran, G. Tytgat, T. Plucinski, J. Paskievitch, and S. R. McNutt (2004), Seismic explorations in the eastern Aleutians, Alaska, *Seismol. Res. Lett.*, *75*, 8–21, doi:10.1785/gssrl.75.1.8.

Christensen, N. I. (1996), Poisson's ratio and crustal seismology, *J. Geophys. Res.*, *101*, 3139–3156, doi:10.1029/95JB03446.

Christensen, N. I., and W. D. Mooney (1995), Seismic velocity structure and composition of the continental crust: A global view, *J. Geophys. Res.*, *100*, 9761–9788, doi:10.1029/95JB00259.

Cross, R. S., and J. T. Freymueller (2008), Evidence for and implications of a Bering plate based on geodetic measurements from the Aleutians and western Alaska, *J. Geophys. Res.*, *113*, B07405, doi:10.1029/2007JB005136.

Dehn, J., K. Dean, and K. Engle (2000), Thermal monitoring of North Pacific volcanoes from space, *Geology*, *28*, 755–758, doi:10.1130/0091-7613(2000)28<755:TMONPV>2.0.CO;2.

Del Negro, C., G. Currenti, and D. Scandura (2009), Temperature-dependent viscoelastic modeling of ground deformation: Application to Etna volcano during the 1993–1997 inflation period, *Phys. Earth Planet. Inter.*, *172*, 299–309, doi:10.1016/j.pepi.2008.10.019.

Dieterich, J. H., and R. W. Decker (1975), Finite element modeling of surface deformation associated with volcanism, *J. Geophys. Res.*, *80*, 4094–4102, doi:10.1029/JB080i029p04094.

Dvorak, J., and A. T. Okamura (1987), A hydraulic model to explain variations in summit tilt rate at Kilauea and Mauna Loa volcanoes, in *Volcanism in Hawaii*, edited by R. W. Decker, T. L. Wright, and P. H. Stauffer, *U.S. Geol. Surv. Prof. Pap., 1350*, 1281–1296.

Finney, B., S. Turner, C. Hawkesworth, J. Larsen, C. Nye, R. Gorge, I. Bindeman, and J. Eichelberger (2008), Magmatic differentiation at an island-arc caldera: Okmok volcano, Aleutian islands, Alaska, *J. Petrol.*, *49*, 857–884, doi:10.1093/petrology/egn008.

Fournelle, J., B. D. Marsh, and J. D. Myers (1994), Age, character and significance of Aleutian arc volcanism, in *The Geology of North America*, vol. G-1, *The Geology of Alaska*, edited by G. Plafker and H. C. Berg, pp. 723–757, Geol. Soc. of Am., Boulder, Colo.

Fournier, T., J. Freymueller, and P. Cervelli (2009), Tracking magma volume recovery at Okmok volcano using GPS and an unscented Kalman filter, *J. Geophys. Res.*, *114*, B02405, doi:10.1029/2008JB005837.

Freymueller, J. T., and A. M. Kaufman (2010), Changes in the magma system during the 2008 eruption of Okmok volcano, Alaska, based on GPS measurements, *J. Geophys. Res.*, *115*, B12415, doi:10.1029/2010JB007716.

Haney, M. M. (2010), Location and mechanism of very long period tremor during the 2008 eruption of Okmok Volcano from interstation arrival times, *J. Geophys. Res.*, *115*, B00B05, doi:10.1029/2010JB007440.

House, L. S., and K. H. Jacob (1983), Earthquakes, plate subduction, and stress reversals in the eastern Aleutian arc, *J. Geophys. Res.*, *88*, 9347–9373, doi:10.1029/JB088iB11p09347.

Huebner, K. H., D. L. Dewhirst, D. E. Smith, and T. G. Byrom (2001), *The Finite Element Method for Engineers*, 720 pp., John Wiley, New York.

Izbekov, P. E., J. F. Larsen, and J. E. Gardner (2005), Petrological and experimental constraints on the recent magma plumbing system at Okmok volcano, Alaska, USA, *Eos Trans. AGU*, *86*(52), Fall Meet. Suppl., Abstract V13B-0533.

Jaeger, J. C. (1956), *Elasticity, Fracture and Flow With Engineering and Geological Applications*, edited by B. L. Worsnop, Methuen, London.

Jaeger, J. C., N. G. W. Cook, and R. W. Zimmerman (2007), *Fundamentals of Rock Mechanics*, 4th ed., 475 pp., Blackwell, Malden, Mass.

Jellinek, A. M., and D. J. DePaolo (2003), A model for the origin of large silicic magma chambers: Precursors of caldera-forming eruptions, *Bull. Volcanol.*, *65*, 363–381, doi:10.1007/s00445-003-0277-y.

Johnson, J. H., S. Prejean, M. K. Savage, and J. Townend (2010), Anisotropy, repeating earthquakes, and seismicity associated with the 2008 eruption of Okmok volcano, Alaska, *J. Geophys. Res.*, *115*, B00B04, doi:10.1029/2009JB006991.

Kinoshita, W. T., R. Y. Koanagi, T. L. Wright, and R. S. Fiske (1969), Kilauea volcano: The 1967–68 summit eruption, *Science*, *166*, 459–468, doi:10.1126/science.166.3904.459.

Larsen, J. F., C. A. Neal, J. R. Schaefer, J. E. Beget, and C. J. Nye (2007), Late Pleistocene and Holocene caldera-forming eruptions of Okmok caldera, Aleutian islands, Alaska, in *Volcanism and Subduction: The Kamchatka Region*, *Geophys. Monogr. Ser.*, vol. 172, edited by J. Eichelberger et al., pp. 343–363, AGU, Washington, D. C., doi:10.1029/172GM24.

Larsen, J., C. Neal, P. Webley, J. Freymueller, M. Haney, S. McNutt, D. Schneider, S. Prejean, J. Schaefer, and R. Wessels (2009), Eruption of Alaska volcano breaks historic pattern, *Eos Trans. AGU*, *90*, 173–180, doi:10.1029/2009EO200001.

Larsen, R. J., and M. L. Marx (1986), *An Introduction to Mathematical Statistics and Its Applications*, 630 pp., Prentice-Hall, Englewood Cliffs, N. J.

Lohman, R. B., and M. Simons (2005), Some thoughts on the use of InSAR data to constrain models of surface deformation: Noise structure and data downsampling, *Geochem. Geophys. Geosyst.*, *6*, Q01007, doi:10.1029/2004GC000841.

Lu, Z. (2007), InSAR imaging of volcanic deformation over cloud-prone areas-Aleutian islands, *Photogramm. Eng. Remote Sens.*, *73*, 245–257.

Lu, Z., and D. Dzurisin (2010), Ground surface deformation patterns, magma supply, and magma storage at Okmok volcano, Alaska, from InSAR analysis: 2. Coeruptive deflation, July–August 2008, *J. Geophys. Res.*, *115*, B00B03, doi:10.1029/2009JB006970.

Lu, Z., D. Mann, J. T. Freymueller, and D. J. Meyer (2000), Synthetic aperture radar interferometry of Okmok volcano, Alaska: Radar observations, *J. Geophys. Res.*, *105*, 10,791–10,806, doi:10.1029/2000JB900034.

Lu, Z., E. Fielding, M. R. Patrick, and C. M. Trautwein (2003), Estimating lava volume by precision combination of multiple baseline spaceborne and airborne interferometric synthetic aperture radar: The 1997 eruption of Okmok volcano, Alaska, *IEEE Trans. Geosci. Remote Sens.*, *41*, 1428–1436.

Lu, Z., T. Masterlark, and D. Dzurisin (2005), Interferometric synthetic aperture study of Okmok volcano, Alaska: Magma supply dynamics and post-emplacement lava flow deformation, *J. Geophys. Res.*, *110*, B02403, doi:10.1029/2004JB003148.

Lu, Z., D. Dzurisin, J. Biggs, C. Wicks Jr., and S. McNutt (2010), Ground surface deformation patterns, magma supply, and magma storage at Okmok volcano, Alaska, from InSAR analysis: 1. Intereruption deformation, 1997–2008, *J. Geophys. Res.*, *115*, B00B02, doi:10.1029/2009JB006969.

Lundgren, P., and P. A. Rosen (2003), Source model for the 2001 flank eruption of Mt. Etna volcano, *Geophys. Res. Lett.*, *30*(7), 1388, doi:10.1029/2002GL016774.

Mann, D., J. Freymueller, and Z. Lu (2002), Deformation associated with the 1997 eruption of Okmok volcano, Alaska, *J. Geophys. Res.*, *107*(B4), 2072, doi:10.1029/2001JB000163.

Massonnet, D., and K. Feigl (1998), Radar interferometry and its application to changes in the Earth's surface, *Rev. Geophys.*, *36*, 441–500, doi:10.1029/97RG03139.

Masterlark, T. (2003), Finite element model predictions of static deformation from dislocation sources in a subduction zone: Sensitivities to homogeneous, isotropic, Poisson-solid, and half-space assumptions, *J. Geophys. Res.*, *108*(B11), 2540, doi:10.1029/2002JB002296.

Masterlark, T. (2007), Magma intrusion and deformation predictions: Sensitivities to the Mogi assumptions, *J. Geophys. Res.*, *112*, B06419, doi:10.1029/2006JB004860.

Masterlark, T., and K. L. H. Hughes (2008), Next generation of deformation models for the 2004 M9 Sumatra-Andaman earthquake, *Geophys. Res. Lett.*, *35*, L19310, doi:10.1029/2008GL035198.

Masterlark, T., Z. Lu, and R. Rykhus (2006), Thickness distribution of a cooling pyroclastic flow deposit: Optimization using InSAR, FEMs, and an adaptive mesh algorithm, *J. Volcanol. Geotherm. Res.*, *150*, 186–201, doi:10.1016/j.jvolgeores.2005.07.004.

Masterlark, T., M. Haney, H. Dickinson, T. Fournier, and C. Searcy (2010), Rheologic and structural controls on the deformation of Okmok volcano, Alaska: FEMS, InSAR and ambient noise tomography, *J. Geophys. Res.*, *115*, B02409, doi:10.1029/2009JB006324.

McGimsey, R. G., and K. L. Wallace (1999), 1997 volcanic activity in Alaska and Kamchatka: Summary of events and response of the Alaska Volcano Observatory, *U.S. Geol. Surv. Open File Rep.*, *OF 99-0448*, 42 pp.

McTigue, D. F. (1987), Elastic stress and deformation near a finite spherical magma body: Resolution of the point source paradox, *J. Geophys. Res.*, *92*, 12,931–12,940, doi:10.1029/JB092iB12p12931.

Menke, W. (1989), *Geophysical Data Analysis: Discrete Inverse Theory*, *Int. Geophys. Ser.*, vol. 45, 289 pp., Academic, San Diego, Calif.

Miller, T. P., R. G. McGimsey, D. H. Richter, J. R. Riehle, C. J. Nye, M. E. Yount, and J. A. Dumoulin (1998), Catalog of the historically active volcanoes of Alaska, *U.S. Geol. Surv. Open File Rep.*, *98-582*, 104 pp.

Miyagi, Y., J. T. Freymueller, F. Kimata, T. Sato, and D. Mann (2004), Surface deformation caused by shallow magmatic activity at Okmok volcano, Alaska, detected by GPS campaigns 2000–2002, *Earth Planets Space*, *56*, e29–e32.

Mogi, K. (1958), Relations between the eruptions of various volcanoes and the deformations of the ground surface around them, *Bull. Earthquake Res. Inst. Univ. Tokyo*, *36*, 99–134.

Newman, A. V., T. H. Dixon, and N. Gourmelen (2006), A four-dimensional viscoelastic model for Long Valley Caldera, California, between 1995 and 2000, *J. Volcanol. Geotherm. Res.*, *150*, 244–269, doi:10.1016/j.jvolgeores.2005.07.017.

Okada, Y. (1992), Internal deformation due to shear and tensile faults in a half-space, *Bull. Seismol. Soc. Am.*, *82*, 1018–1040.

Parthasarathy, V. N., C. M. Graichen, and A. F. Hathaway (1994), A comparison of tetrahedron quality measures, *Finite Elem. Anal. Des.*, *15*, 255–261, doi:10.1016/0168-874X(94)90033-7.

Patrick, M. R., J. Dehn, and K. Dean (2004), Numerical modeling of lava flow cooling applied to the 1997 Okmok eruption: Approach and analysis, *J. Geophys. Res.*, *109*, B03202, doi:10.1029/2003JB002537.

Press, W. H., S. A. Teukolsky, W. T. Vetterling, and B. P. Flannery (2007), *Numerical Recipes: The Art of Scientific Computing*, 3rd ed., 1235 pp., Cambridge Univ. Press, New York.

Sadd, M. H. (2010), *Elasticity—Theory, Applications, and Numerics*, 551 pp., Elsevier, Burlington, Mass.

Segall, P. (2010), *Earthquake and Volcano Deformation*, 432 pp., Princeton Univ. Press, Princeton, N. J.

Shirzaei, M., and T. R. Walter (2007), Randomly iterated search and statistical competency as powerful inversion tools for deformation source modeling: Application to volcano interferometric synthetic aperture radar data, *J. Geophys. Res.*, *114*, B10401, doi:10.1029/2008JB006071.

Simmons, G., and W. F. Brace (1965), Comparison of static and dynamic measurements of compressibility of rocks, *J. Geophys. Res.*, *70*, 5649–5656, doi:10.1029/JZ070i022p05649.

Turcotte, D. L., and G. J. Schubert (2002), *Geodynamics: Applications of Continuum Physics to Geological Problems*, 2nd ed., 456 pp., Cambridge Univ. Press, New York.

Vasco, D. W., C. Wicks Jr., K. Karasaki, and O. Marques (2002), Geodetic imaging: Reservoir monitoring using satellite interferometry, *Geophys. J. Int.*, *149*, 555–571, doi:10.1046/j.1365-246X.2002.01569.x.

Walker, G. P. (1993), Basaltic-volcano systems, in *Magmatic Processes and Plate Tectonics*, edited by H. M. Prichard et al., *Geol. Soc. Spec. Publ.*, *76*, 3–38.

Walpole, R. E., R. H. Myers, S. L. Myers, and K. Ye (2007), *Probability and Statistics for Engineers and Scientists*, 816 pp., Prentice Hall, Upper Saddle River, N. J.

Wang, H. F. (2000), *Theory of Linear Poroelasticity: With Applications to Geomechanics*, 287 pp., Princeton Univ. Press, Princeton, N. J.

Wang, H. F., and M. P. Anderson (1982), *Introduction to Groundwater Modeling: Finite Differences and Finite Element Methods*, 237 pp., Academic, San Diego, Calif.

Williams, C. A., and G. Wadge (1998), The effects of topography on magma chamber deformation models: Application to Mt. Etna and radar interferometry, *Geophys. Res. Lett.*, *25*, 1549–1552, doi:10.1029/98GL01136.

Wright, T., C. Ebinger, J. Biggs, A. Ayele, G. Yirgu, D. Keir, and A. Stork (2006), Magma-maintained rift segmentation at continental rupture in the 2005 Afar dyking episode, *Nature*, *442*, 291–294, doi:10.1038/nature04978.

Yang, X. M., P. M. Davis, and J. H. Deiterich (1988), Deformation from inflation of a dipping finite prolate spheroid in an elastic half-space as a model for volcanic stressing, *J. Geophys. Res.*, *93*, 4249–4257, doi:10.1029/JB093iB05p04249.

Zuo, J., X. Deng, and M. A. Sutton (2005), Advances in tetrahedral mesh generation for modelling of three-dimensional regions with complex, curvilinear crack shapes, *Int. J. Numer. Methods Eng.*, *63*, 256–275, doi:10.1002/nme.1285.

K. L. Feigl and C. Thurber, Department of Geoscience, University of Wisconsin–Madison, Madison, WI 53706, USA.

M. Haney, Alaska Volcano Observatory, U.S. Geological Survey, Anchorage, AK 99508, USA.

T. Masterlark and J. Stone, Department of Geological Sciences, University of Alabama, Tuscaloosa, AL 35487, USA. (masterlark@ua.edu)

E. Ronchin, Institute of Earth Sciences Jaume Almera, CSIC, E-08028 Barcelona, Spain.